U.S. Department
of Transportation
**Federal Railroad
Administration**

Experimental Study of Residual Stresses in Rail by Moire Interferometry

Office of Policy
Washington, DC 20590

Y. Y. Wang
F. P. Chiang

Laboratory for Experimental Mechanics Research
Department of Mechanical Engineering
State University of New York at Stony Brook
Stony Brook, NY 11794-2300

DOT/FRA/ORD-94/02
DOT/VNTSC-FRA-93-24

Final Report
September 1993

NOTICE

This document is disseminated under the sponsorship of the Department of Transportation in the interest of information exchange. The United States Government assumes no liability for its contents or use thereof.

NOTICE

The United States Government does not endorse products or manufacturers. Trade or manufacturers' names appear herein solely because they are considered essential to the object of this report.

NOTICE

In places, this report discusses whether various aspects of the technology that is the subject of this report comply with Federal safety laws and regulations. Those discussions, which reflect the seasoned judgement of commentators qualified in their fields, do not constitute rulings by the Federal Railroad Administration's Office of Safety or its Office of Chief Counsel concerning compliance with the law.

REPORT DOCUMENTATION PAGE

Form Approved
OMB No. 0704-0188

1. AGENCY USE ONLY (Leave blank)	2. REPORT DATE	3. REPORT TYPE AND DATES COVERED
	September 1993	Final Report January 1992-January 1993

4. TITLE AND SUBTITLE
Experimental Study of Residual Stresses in Rail by Moire Interferometry

5. FUNDING NUMBERS
R3001/RR319

6. AUTHOR(S)
Y. Y. Wang and F.P. Chiang

7. PERFORMING ORGANIZATION NAME(S) AND ADDRESS(ES)
Laboratory for Experimental Mechanics Research
Department of Mechanical Engineering
State University of New York at Stony Brook
Stony Brook, NY 11794-2300

8. PERFORMING ORGANIZATION REPORT NUMBER
DOT-VNTSC-FRA-93-24

9. SPONSORING/MONITORING AGENCY NAME(S) AND ADDRESS(ES)
U.S. Department of Transportation
Federal Railroad Administration
Office of Research and Development
Washington, DC 20590

10. SPONSORING/MONITORING AGENCY REPORT NUMBER
DOT/FRA/ORD-94/02

11. SUPPLEMENTARY NOTES

*under contract to:

U.S. Department of Transportation
Research and Special Programs Administration
John A. Volpe National Transportation Systems Center
55 Broadway
Kendall Square, Cambridge, MA 02142

12a. DISTRIBUTION/AVAILABILITY STATEMENT
This document is available to the public through the National Technical Information Service, Springfield, VA 22161

12b. DISTRIBUTION CODE

13. ABSTRACT (Maximum 200 words)

A moire interferometry technique is used to measure the residual stresses in railroad rails. The moire is applied to the faces of transverse and oblique slices cut from each of two rails. An orthogonal network of cuts is then made in each slice, in order to release the remnant in-plane stresses, and the resulting moire fringe fields are recorded. Release strains and stresses are determined from the fringe spacings and Hooke's law, respectively. A simple tensor transformation is applied to the transverse and oblique plane strains in order to estimate the axial normal stress component. This estimation procedure is based on the assumptions that the rail residual stress field is axially uniform, and that only a small percentage of the in-plane stress is released (and thus not measured) by cutting the slices from the rail. The experimental procedure is shown to be workable, although the cut network requires a long time to produce. Other problems associated with the cut network are plastic distortion of the remnant blocks (on which the moire fringes are measured) by the cutting tool and the interruption of full-field moire data by the network. An alternate method of heat treatment for stress release instead of cutting is discussed. The axial stresses estimated from the tensor transformation procedure appear to be of the correct order of magnitude when compared with earlier results obtained from other rails by a different technique.

14. SUBJECT TERMS
Moire; Rail; Residual Stress

15. NUMBER OF PAGES
48

16. PRICE CODE

17. SECURITY CLASSIFICATION OF REPORT	18. SECURITY CLASSIFICATION OF THIS PAGE	19. SECURITY CLASSIFICATION OF ABSTRACT	20. LIMITATION OF ABSTRACT
Unclassified	Unclassified	Unclassified	

PREFACE

The Office of Research and Development of the Federal Railroad Administration sponsors a program of research on rail integrity. One of the key findings of this research is that residual stress has a strong influence on the formation and propagation of fatigue cracks in the rail head. Thus, there are important safety and economic reasons for better understanding of the factors which tend to increase or decrease residual stresses in rails. Such understanding requires both a theoretical model to provide a logical framework and experimental results to guide the development of the model.

This report summarizes the results of an investigation of an improved experimental stress analysis procedure. Up to 1990, rail residual stresses were measured solely by means of destructive sectioning with strain gauges and metrological microscopes used to measure quantities from which the released stresses could be estimated. To obtain a comprehensive stress field map with this technique required the cutting of a long rail section, as well as a transverse slice, an extremely labor-intensive approach. The use of moire grating in place of strain gauges, first demonstrated in 1990, opened a pathway to a potentially much cheaper and more accurate approach. The saving of labor and handling problems encountered with strain gauges made it possible to consider, for the first time, working with two slices (one transverse and one oblique) instead of the single transverse slice and long section. The work reported here demonstrates that the alternate procedure is workable, but further improvements of both accuracy and economy are needed to obtain a truly practical method for mapping rail residual stress fields. It appears that the desired procedure can be developed in the next phase of the research program.

METRIC/ENGLISH CONVERSION FACTORS

ENGLISH TO METRIC

LENGTH (APPROXIMATE)

1 inch (in) = 2.5 centimeters (cm)
1 foot (ft) = 30 centimeters (cm)
1 yard (yd) = 0.9 meter (m)
1 mile (mi) = 1.6 kilometers (km)

AREA (APPROXIMATE)

1 square inch (sq in, in^2) = 6.5 square centimeters (cm^2)
1 square foot (sq ft, ft^2) = 0.09 square meter (m_2)
1 square yard (sq yd, yd^2) = 0.8 square meter (m^2)
1 square mile (sq mi, mi^2) = 2.6 square kilometers (km^2)
1 acre = 0.4 hectares (he) = 4,000 square meters (m^2)

MASS - WEIGHT (APPROXIMATE)

1 ounce (oz) = 28 grams (gr)
1 pound (lb) = .45 kilogram (kg)
1 short ton = 2,000 pounds (lb) = 0.9 tonne (t)

VOLUME (APPROXIMATE)

1 teaspoon (tsp) = 5 milliliters (ml)
1 tablespoon (tbsp) = 15 milliliters (ml)
1 fluid ounce (fl oz) = 30 milliliters (ml)
1 cup (c) = 0.24 liter (l)
1 pint (pt) = 0.47 liter (l)
1 quart (qt) = 0.96 liter (l)
1 gallon (gal) = 3.8 liters (l)
1 cubic foot (cu ft, ft^3) = 0.03 cubic meter (m^3)
1 cubic yard (cu yd, yd^3) = 0.76 cubic meter (m^3)

TEMPERATURE (EXACT)

$[(x-32)(5/9)]\ ^{o}F = y\ ^{o}C$

METRIC TO ENGLISH

LENGTH (APPROXIMATE)

1 millimeter (mm) = 0.04 inch (in)
1 centimeter (cm) = 0.4 inch (in)
1 meter (m) = 3.3 feet (ft)
1 meter (m) = 1.1 yards (yd)
1 kilometer (km) = 0.6 mile (mi)

AREA (APPROXIMATE)

1 square centimeter (cm^2) = 0.16 square inch (sq in, in^2)
1 square meter (m^2) = 1.2 square yeards (sq yd, yd^2)
1 square kilometer (km^2) = 0.4 square mile (sq mi, mi^2)
1 hectare (he) = 10,000 square meters (m^2) = 2.5 acres

MASS - WEIGHT (APPROXIMATE)

1 gram (gr) = 0.036 ounce (oz)
1 kilogram (kg) = 2.2 pounds (lb)
1 tonne (t) = 1,000 kilograms (kg) = 1.1 short tons

VOLUME (APPROXIMATE)

1 milliliters (ml) = 0.03 fluid ounce (fl oz)
1 liter (l) = 2.1 pints (pt)
1 liter (l) = 1.06 quarts (qt)
1 liter (l) = 0.26 gallon (gal)
1 cubic meter (m^3) = 36 cubic feet (cu ft, ft^3)
1 cubic meter (m^3) = 1.3 cubic yards (cu yd, yd^3)

TEMPERATURE (EXACT)

$[(9/5)\ y + 32]\ ^{o}C = x\ ^{o}F$

QUICK INCH-CENTIMETER LENGTH CONVERSION

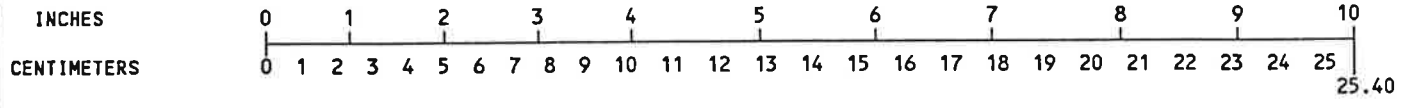

QUICK FAHRENHEIT-CELSIUS TEMPERATURE CONVERSION

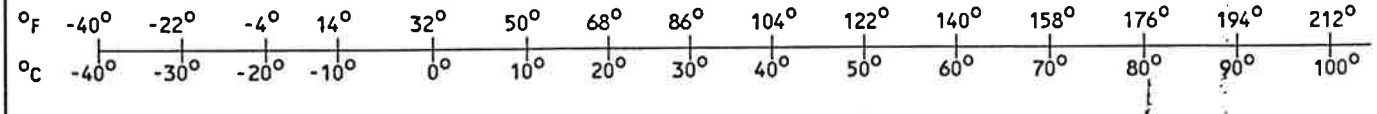

For more exact and or other conversion factors, see NBS Miscellaneous Publication 286, Units of Weights and Measures. Price $2.50. SD Catalog No. C13 10286.

TABLE OF CONTENTS

LIST OF ILLUSTRATIONS

LIST OF ILLUSTRATIONS (continued)

LIST OF ILLUSTRATIONS (continued)

1. INTRODUCTION

The residual stresses in rails produced by rolling cycles are studied experimentally by moire interferometry. The dissection technique is adopted for this investigation. The basic principle of the dissection technique is that the residual stress is released elastically by creating free boundaries when the specimen is cut into small pieces. In this study, instead of cutting small pieces, we cut the rail into thin slices first, and then cut grooves on the surface of the slice to produce many small grid elements with right angles. When the elements are small enough, it is assumed that the edges of the element are the stress free boundaries and thus relax the residual stress near the surface of the slice. The resulting deformation is measured by moire interferometry.

2. EXPERIMENT METHOD

Moire interferometry is a high-sensitivity optical method of measuring in-plane deformations of solid bodies [1]. Figure 1 is the experimental setup used in this investigation. A collimated and coherent laser beam is split into two beams with one impinging on the specimen and the other on the mirror. The beam propagating to the mirror is also reflected onto the specimen. Therefore, there are two plane waves illuminating the specimen grating. The incident angle of the two beams are so arranged that their $\pm$ 1 diffraction orders form the grating surface emerging along the z direction. When the specimen grating is deformed, the wave fronts of the two diffraction beams are warped. It is the interference of these two diffraction beams that results in the forming of the moire fringe pattern. A compound lens is used to collect diffraction beams to form an image of the specimen. The specimen is mounted on a rotation stage which is rotatable about the z axis. The specimen is aligned in such a way that the fringes representing one displacement field, for example the u-field, are recorded first, the specimen is then rotated 90 degrees to allow the formation of the v-field fringes for recording. The rotation stage is controlled by a stepping motor with a minimum step being 0.01 degrees. This rotation stage is also used to perform rotation mismatch when the sign of strain needs to be determined.

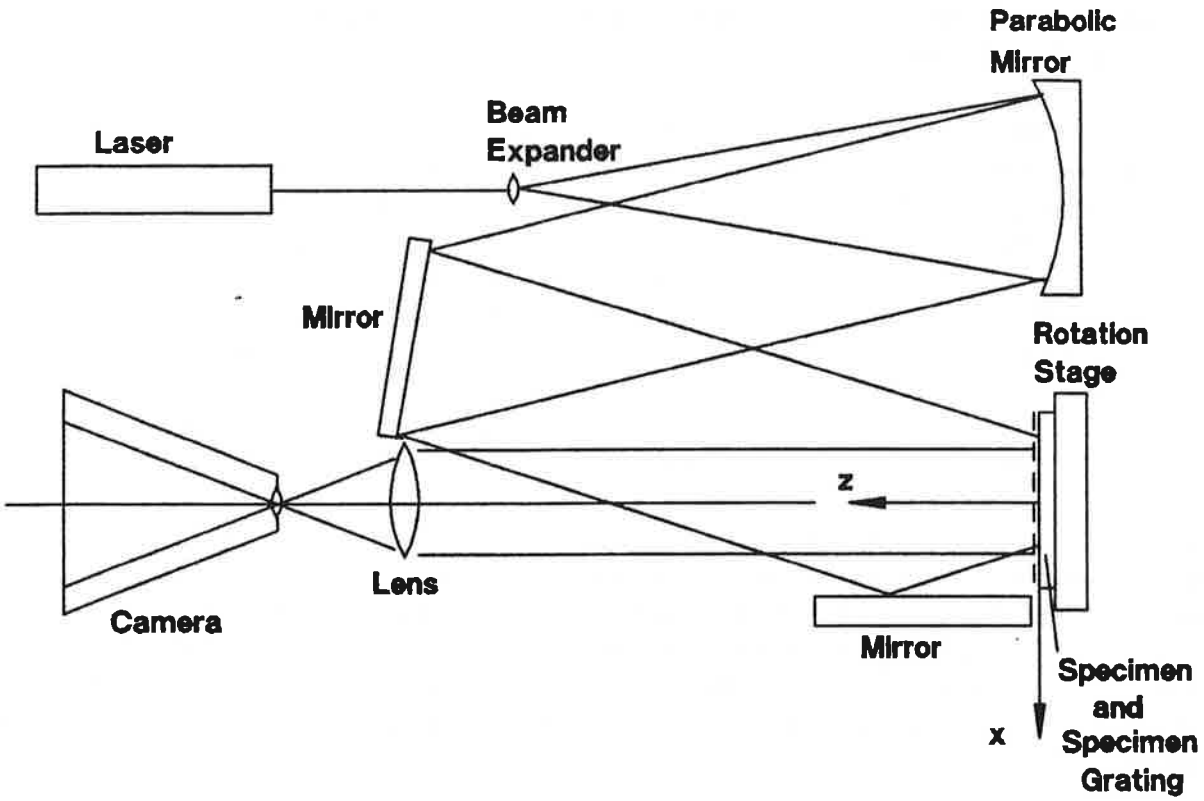

FIGURE 1. THE EXPERIMENTAL SETUP

3. EXPERIMENT PROCEDURE

Two sets of slices are investigated in this study. For each set, one slice is cut perpendicular to the longitudinal direction of the rail and the other is inclined 45 degrees to the rail axis (refer to Figure 2). The cross-sectional surface of each slice is carefully ground flat. The grinding direction is parallel to the x-axis so the top edge of the rail head remains sharp after grinding. A high-frequency (1200 line/mm) cross-line diffraction grating is replicated on each specimen with epoxy PC-10C. The ratio of the hardener and the resin is reduced and a very thin and relatively flexible grating is formed on the flat surface of the slices. Most of the head portion of the rail specimen is covered by the grating and the experiment data are collected over an area about 50 x 30 *mm*.

The specimen is mounted on the rotation stage and is precisely guided with three fixed pins. After the interferometer is adjusted to a null field with the uncut specimen, the specimen is taken to the shop for cutting, while the interferometer is kept in the adjusted position. Cutting is done by a circular diamond blade on a general grinder. Initially, four cuts are made at one corner of the specimen to produce at least one separate grid element. The specimen is brought back to the interferometer and the rotation stage is adjusted till the minimum number of fringes are observed at the uncut region. The resulting fringe pattern is taken. This fringe pattern in the grid element is to be used later, after all other grooves are cut, to calibrate the position of the specimen. This is possible because the displacements in that free grid element should not change with any additional cuts. The cuts are made every 4 *mm* with 4 *mm* to 6 *mm* depth. It is assumed [2] that when the ratio of depth to grid element length is 1 to 1.5, such a depth is sufficient to release most of the residual stresses. To minimize thermal stresses due to machining, the cutting is done with very slow feed rate and the specimen is cooled by a strong vacuum machine. Generally 10 x 15 grid elements are made for each slice. The specimen is then positioned precisely in the interferometer by matching the fringe pattern of the first free element. The u and v displacement fields are then recorded (Figures 3 and 4). For the determination of the sign of strain, rotation mismatch fringes are added to the patterns as shown in Figures 5 and 6.

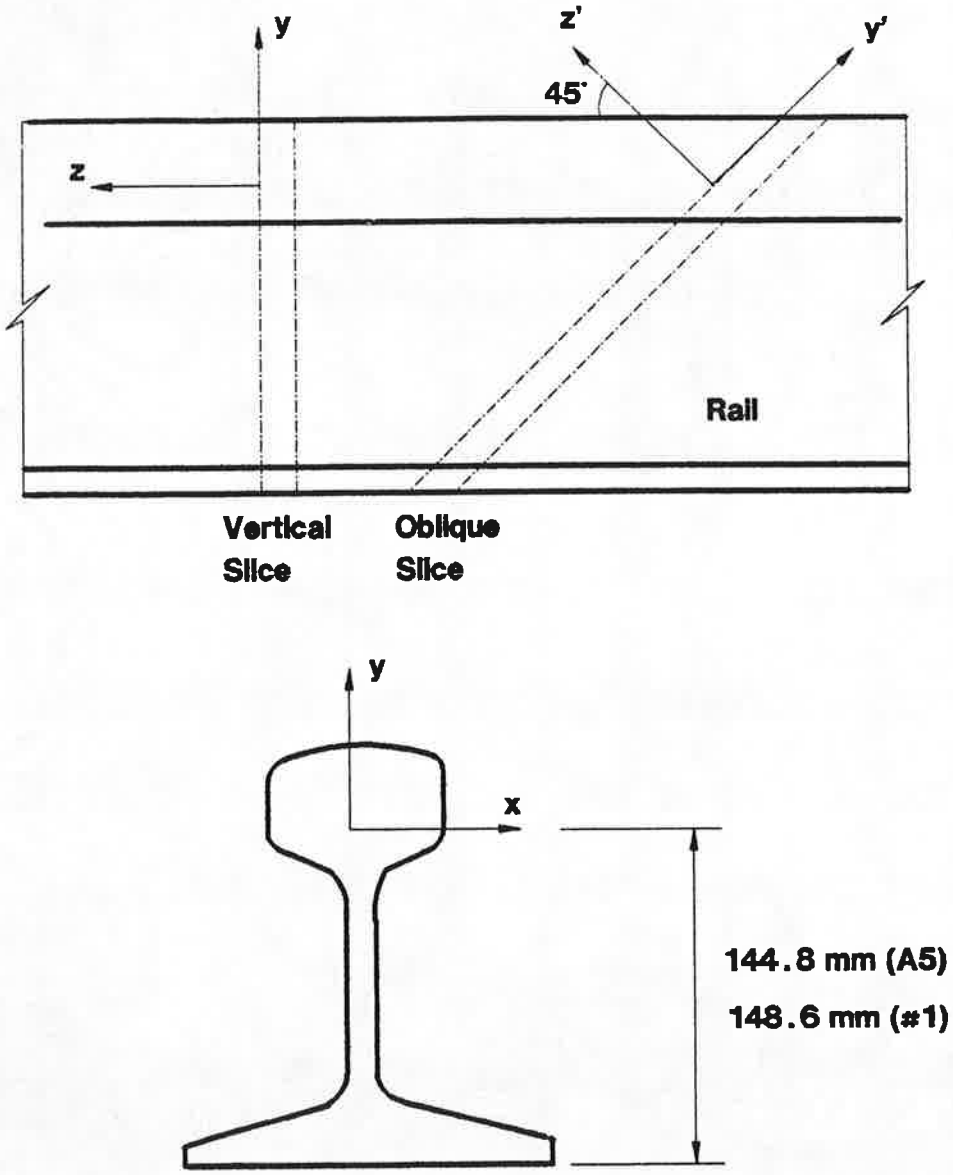

FIGURE 2. ORIENTATION OF THE SLICES

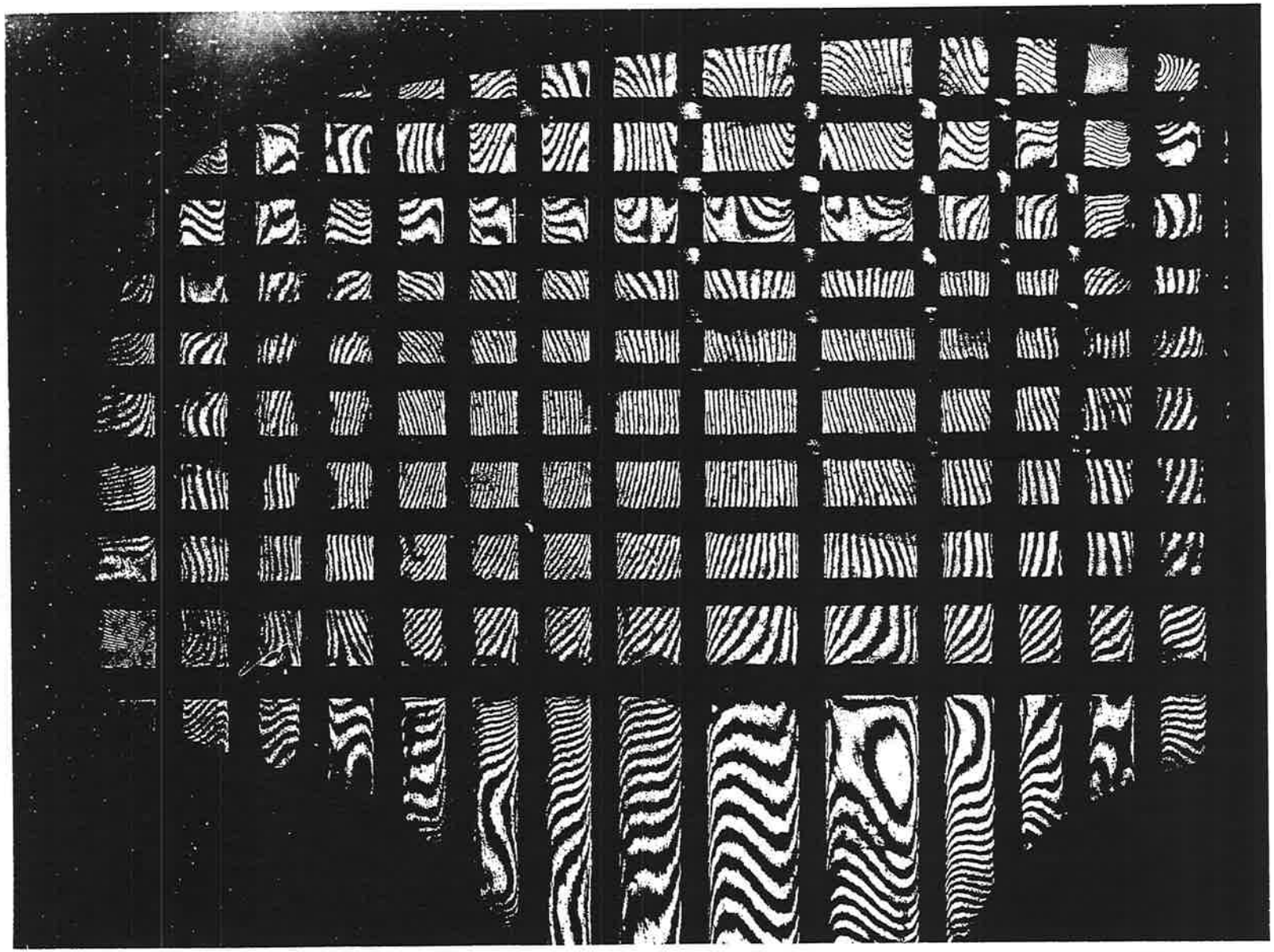

FIGURE 3a. U-FIELD FRINGE PATTERN OF REVEALING THE RESIDUAL DEFORMATION IN X-DIRECTION OF RAIL A5 (VERTICAL SLICE)

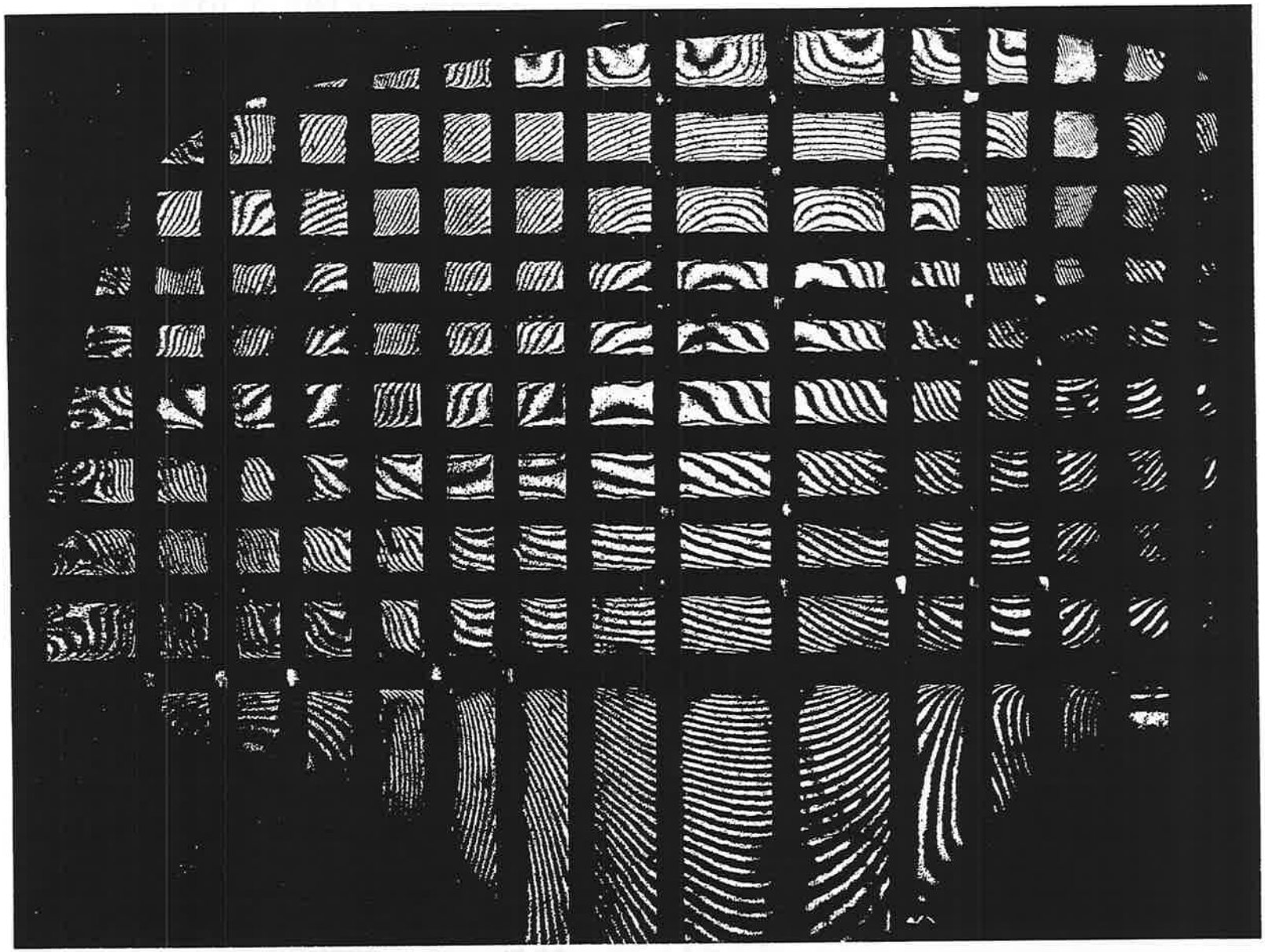

FIGURE 3b. V-FIELD FRINGE PATTERN OF REVEALING THE RESIDUAL DEFORMATION IN Y-DIRECTION OF RAIL A5 (VERTICAL SLICE)

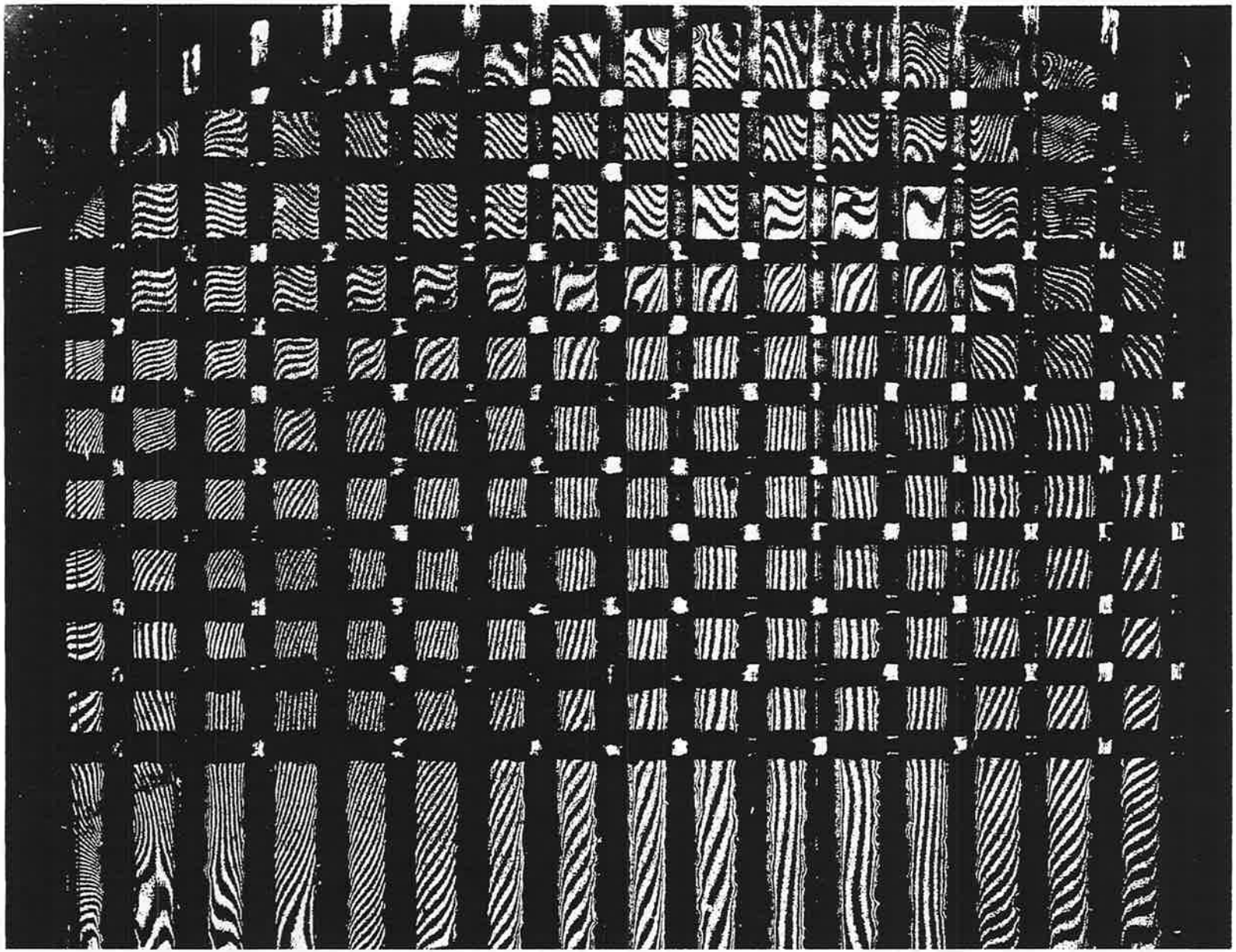

FIGURE 3c. U-FIELD FRINGE PATTERN OF REVEALING THE RESIDUAL DEFORMATION IN X-DIRECTION OF RAIL A5 (OBLIQUE SLICE)

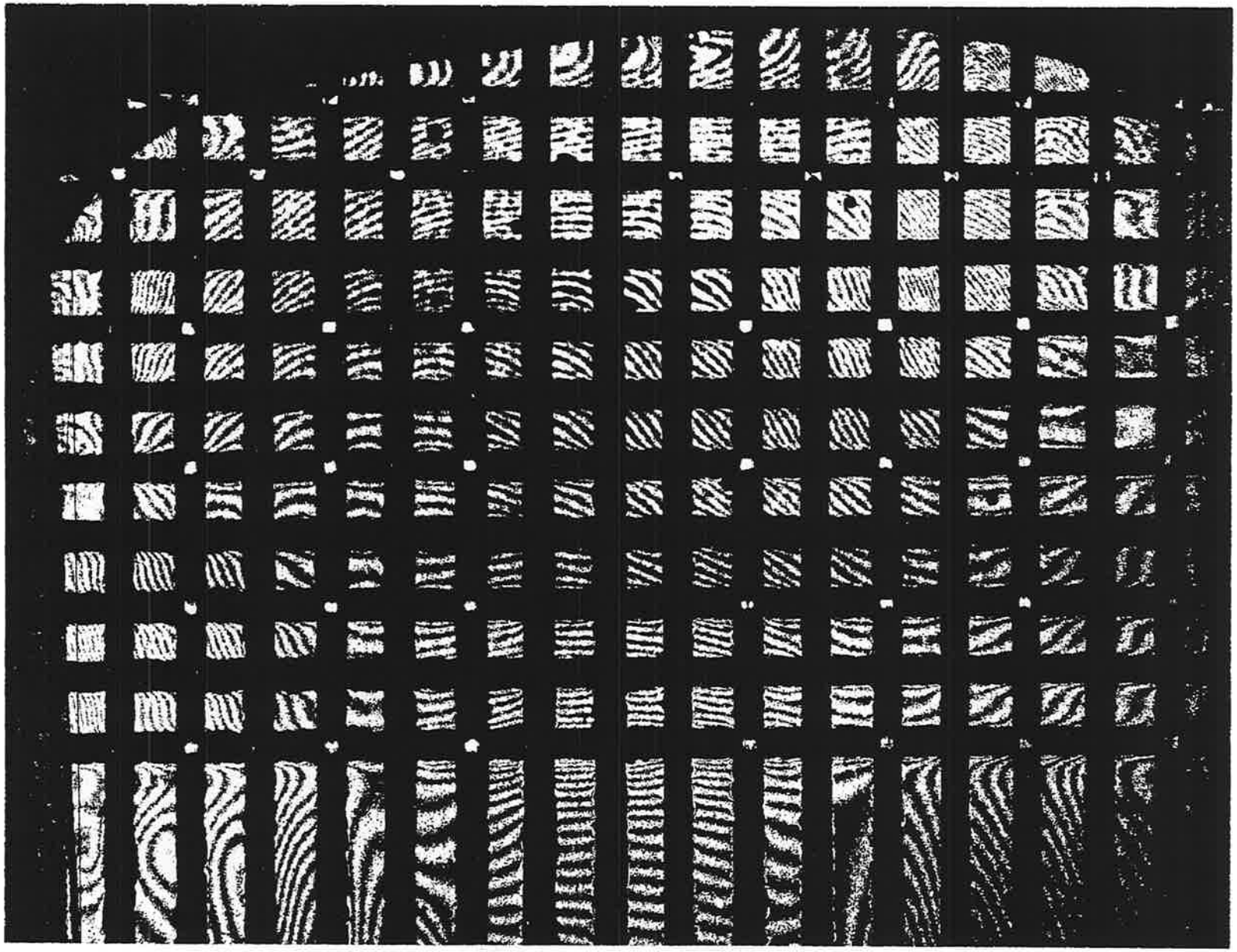

FIGURE 3d. V-FIELD FRINGE PATTERN OF REVEALING THE RESIDUAL DEFORMATION IN Y-DIRECTION OF RAIL A5 (OBLIQUE SLICE)

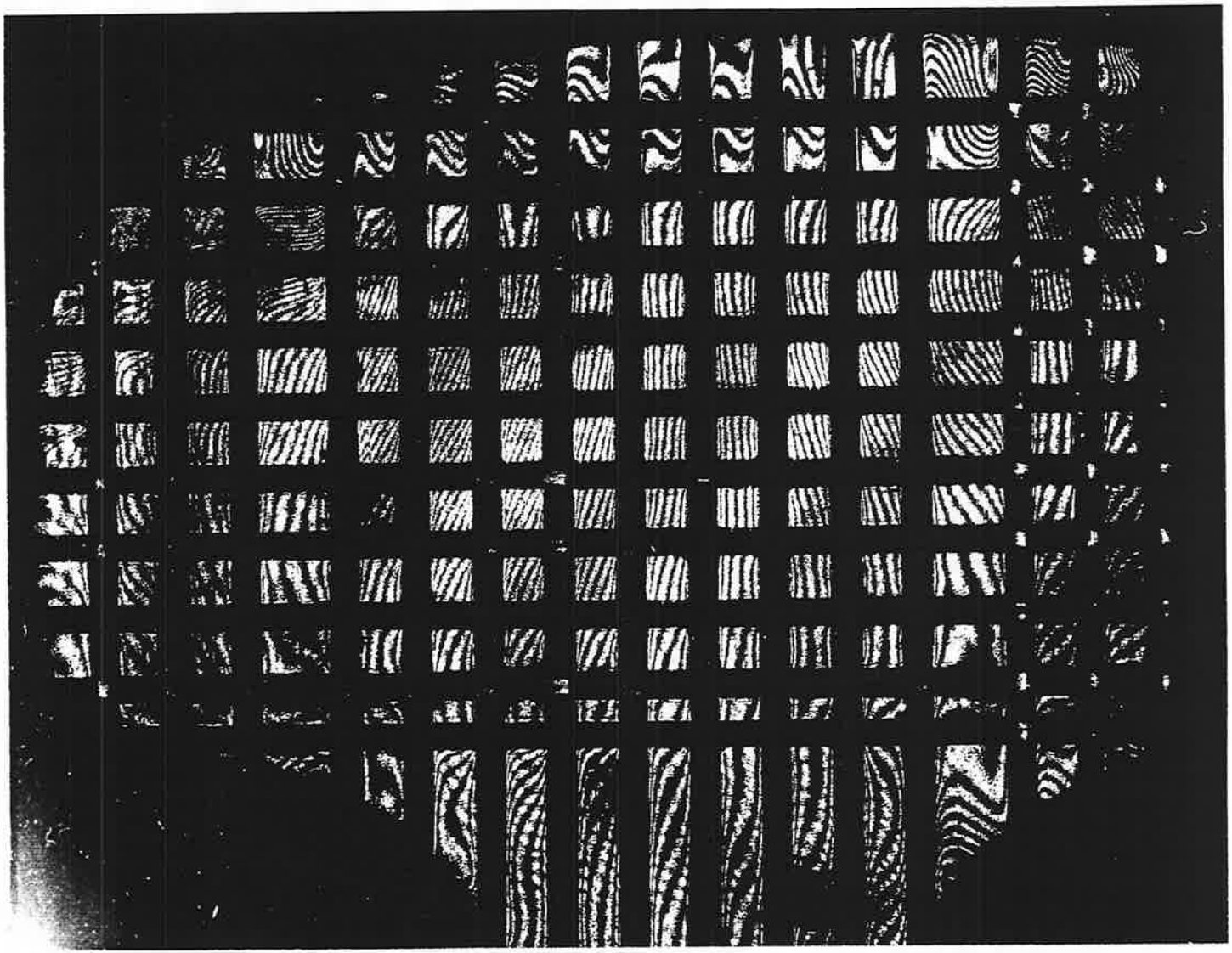

FIGURE 4a. U-FIELD FRINGE PATTERN OF REVEALING THE RESIDUAL DEFORMATION IN X-DIRECTION OF RAIL #1 (VERTICAL SLICE)

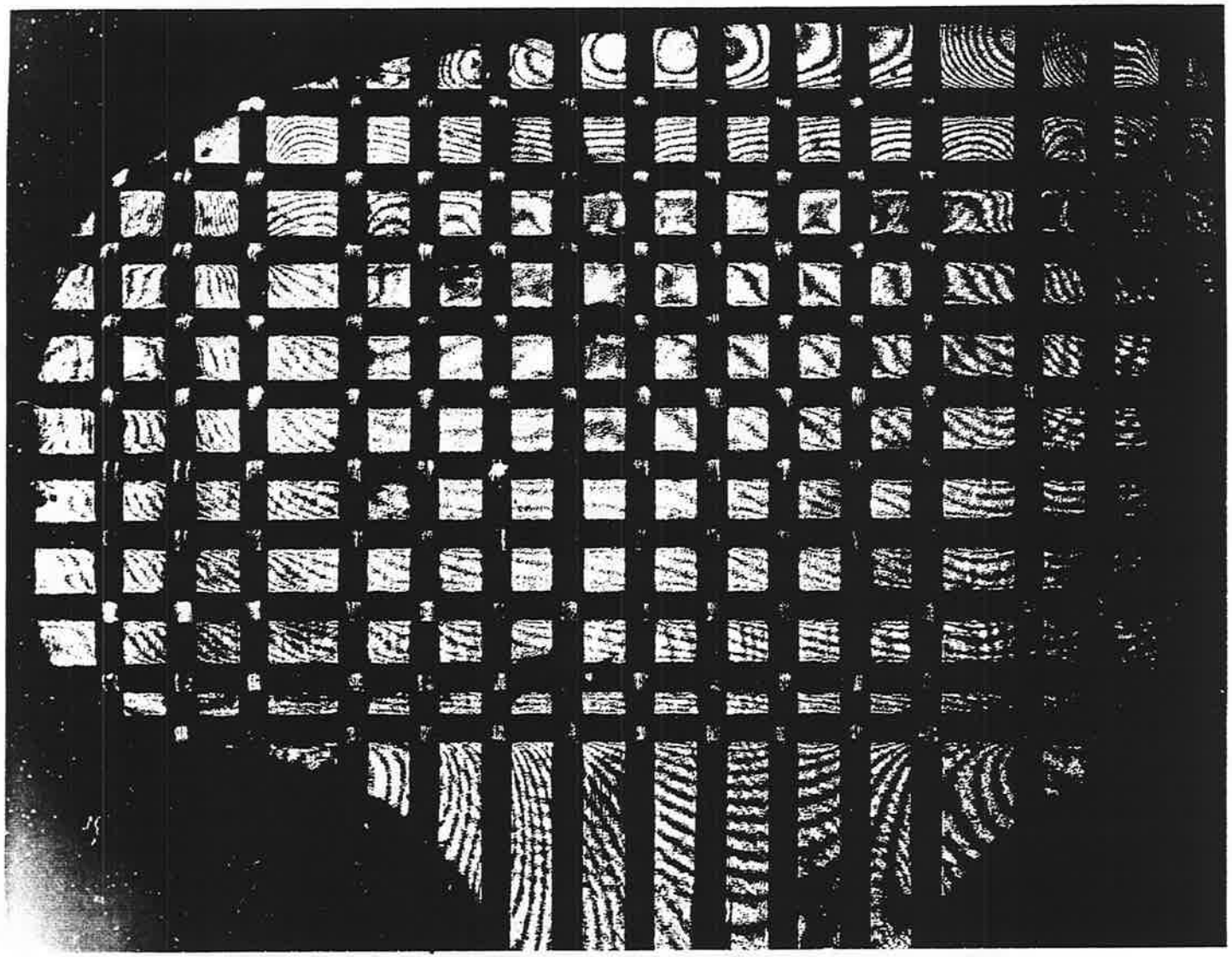

FIGURE 4b. V-FIELD FRINGE PATTERN OF REVEALING THE RESIDUAL DEFORMATION IN Y-DIRECTION OF RAIL #1 (VERTICAL SLICE)

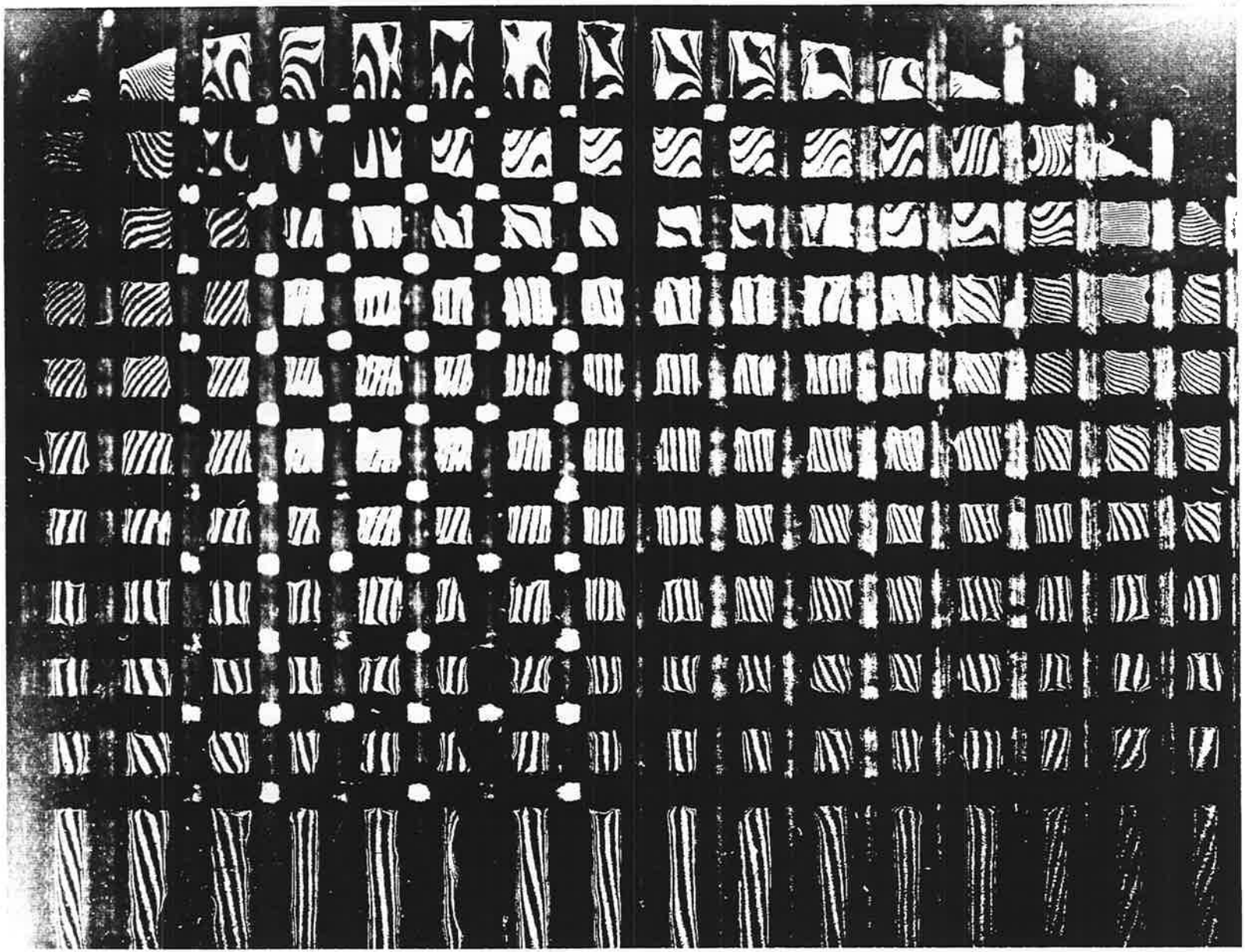

FIGURE 4c. U-FIELD FRINGE PATTERN OF REVEALING THE RESIDUAL DEFORMATION IN X-DIRECTION OF RAIL #1 (OBLIQUE SLICE)

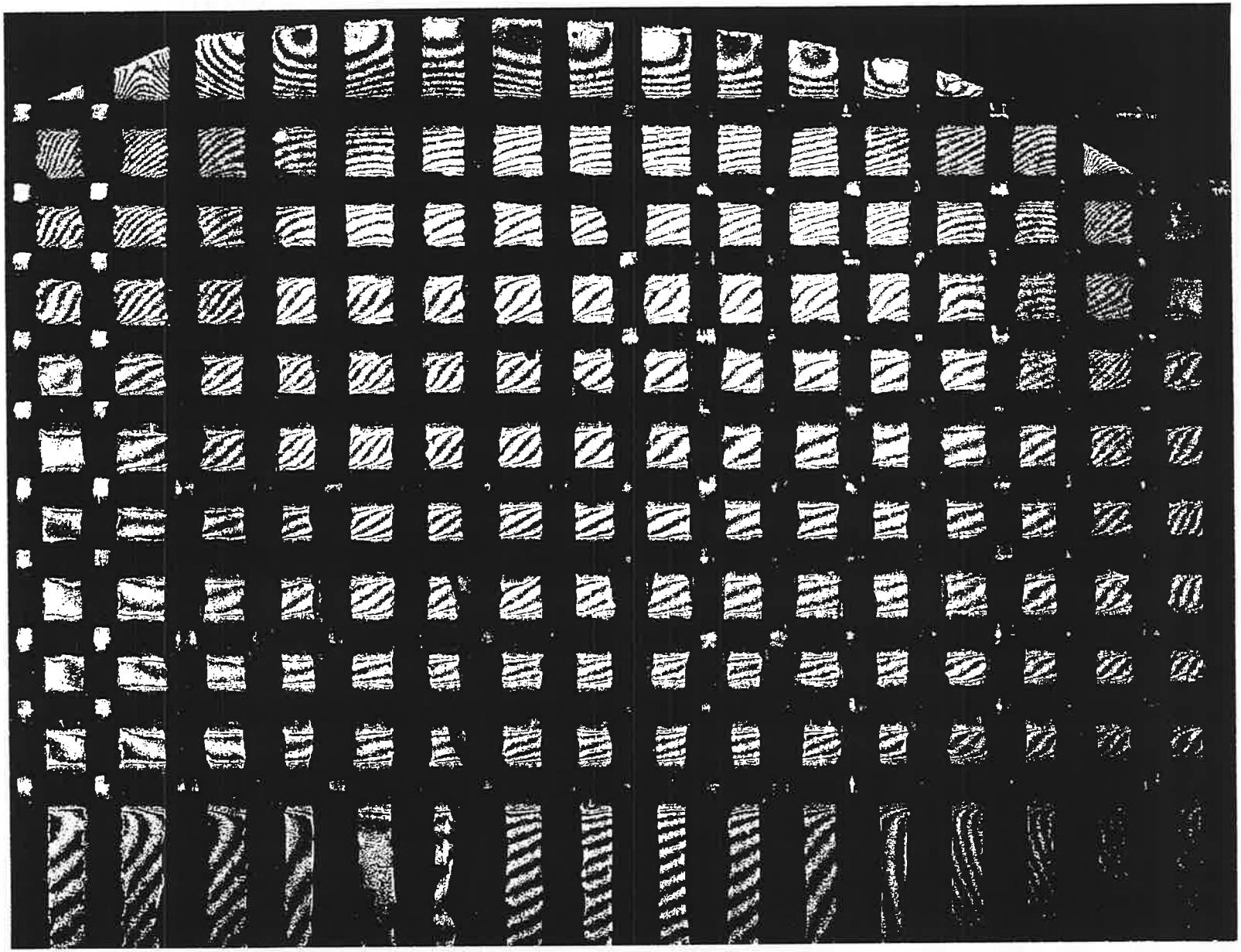

FIGURE 4d. V-FIELD FRINGE PATTERN OF REVEALING THE RESIDUAL DEFORMATION IN Y-DIRECTION OF RAIL #1 (OBLIQUE SLICE)

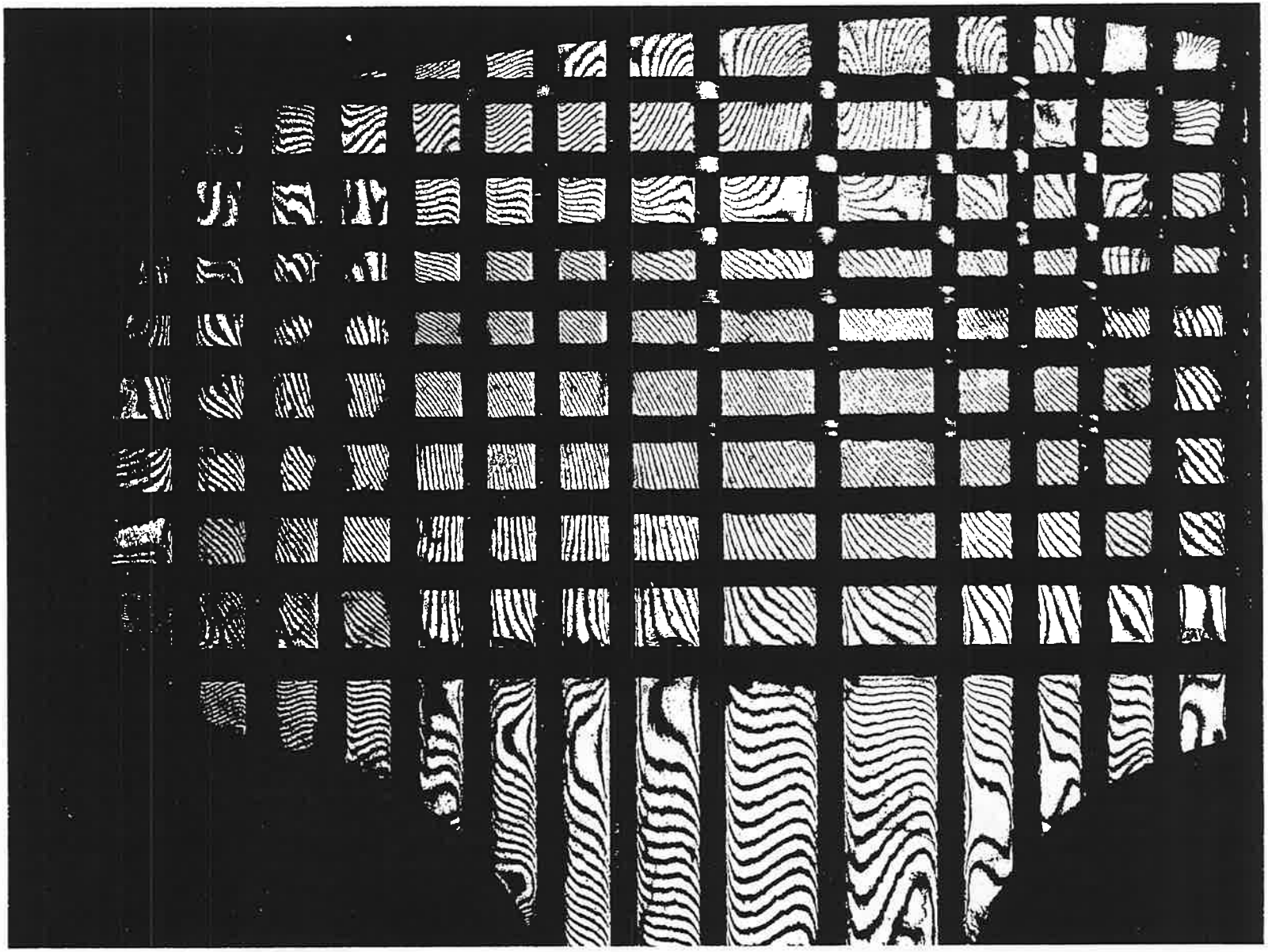

FIGURE 5a. U-FIELD FRINGE PATTERN WITH ROTATION MISMATCH FRINGES FOR THE DETERMINATION OF STRAIN SIGNS (RAIL A5, VERTICAL SLICE)

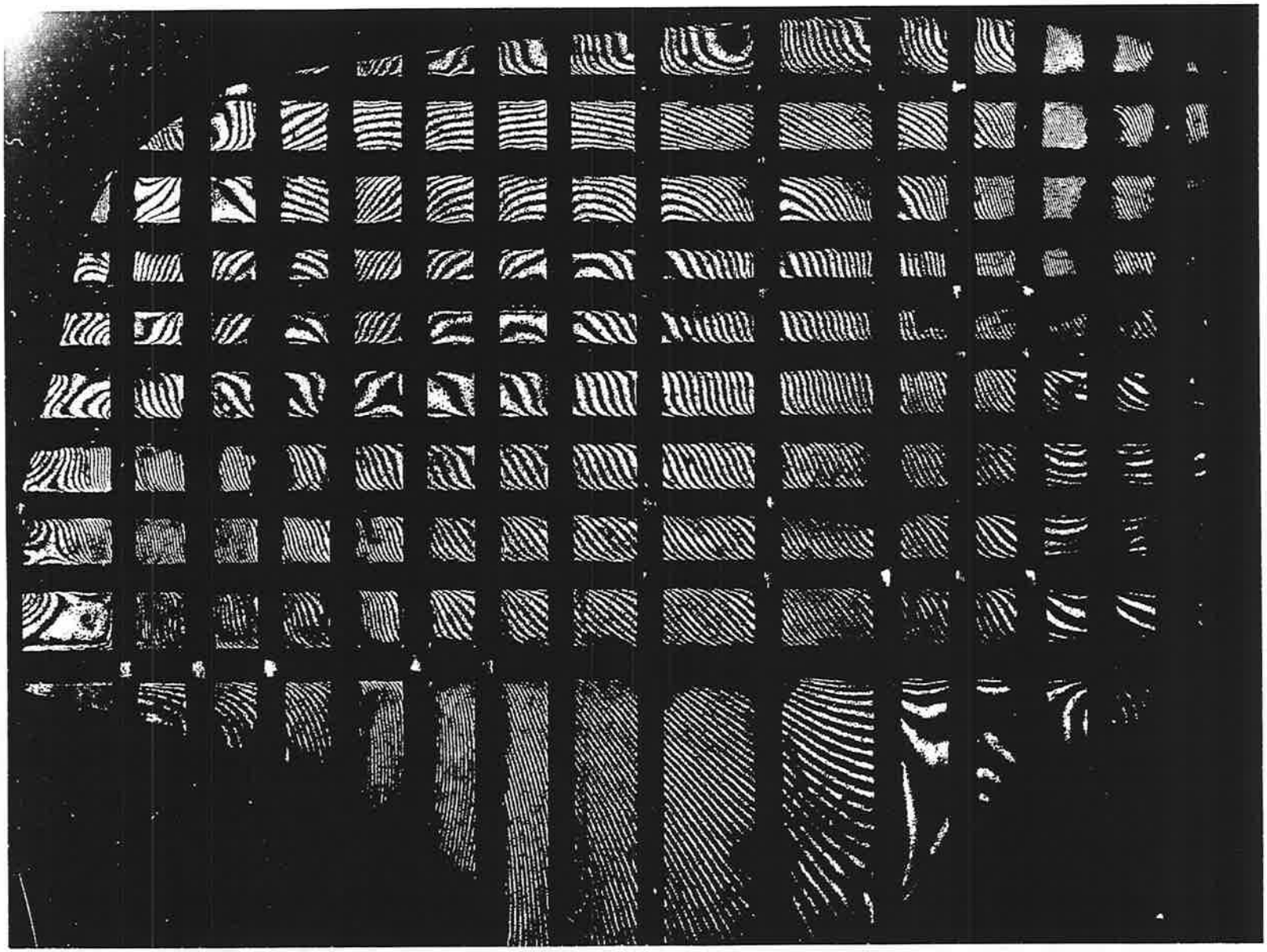

FIGURE 5b. V-FIELD FRINGE PATTERN WITH ROTATION MISMATCH FRINGES FOR THE DETERMINATION OF STRAIN SIGNS (RAIL A5, VERTICAL SLICE)

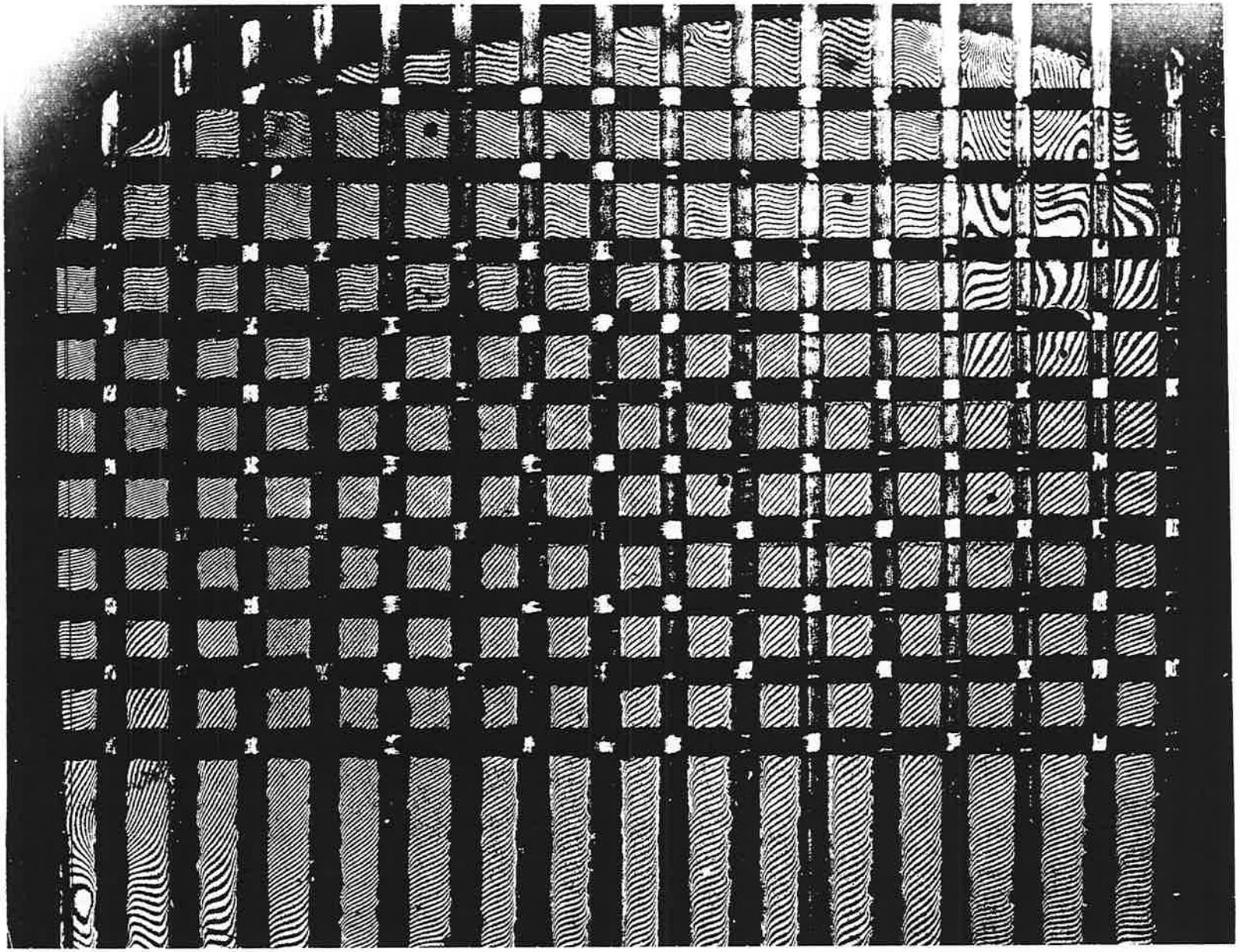

FIGURE 5c. U-FIELD FRINGE PATTERN WITH ROTATION MISMATCH FRINGES FOR THE DETERMINATION OF STRAIN SIGNS (RAIL A5, OBLIQUE SLICE)

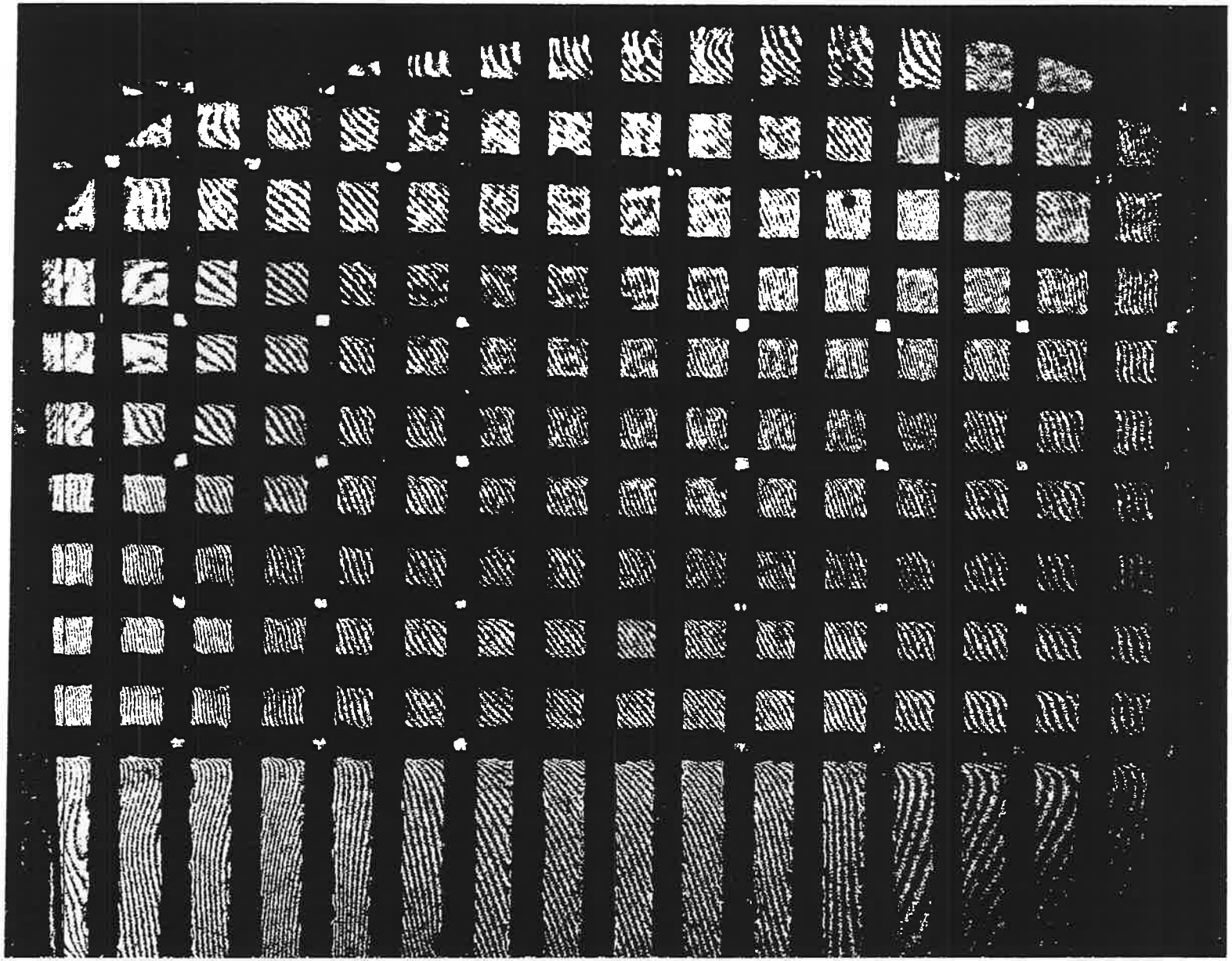

FIGURE 5d. V-FIELD FRINGE PATTERN WITH ROTATION MISMATCH FRINGES FOR THE DETERMINATION OF STRAIN SIGNS (RAIL A5, OBLIQUE SLICE)

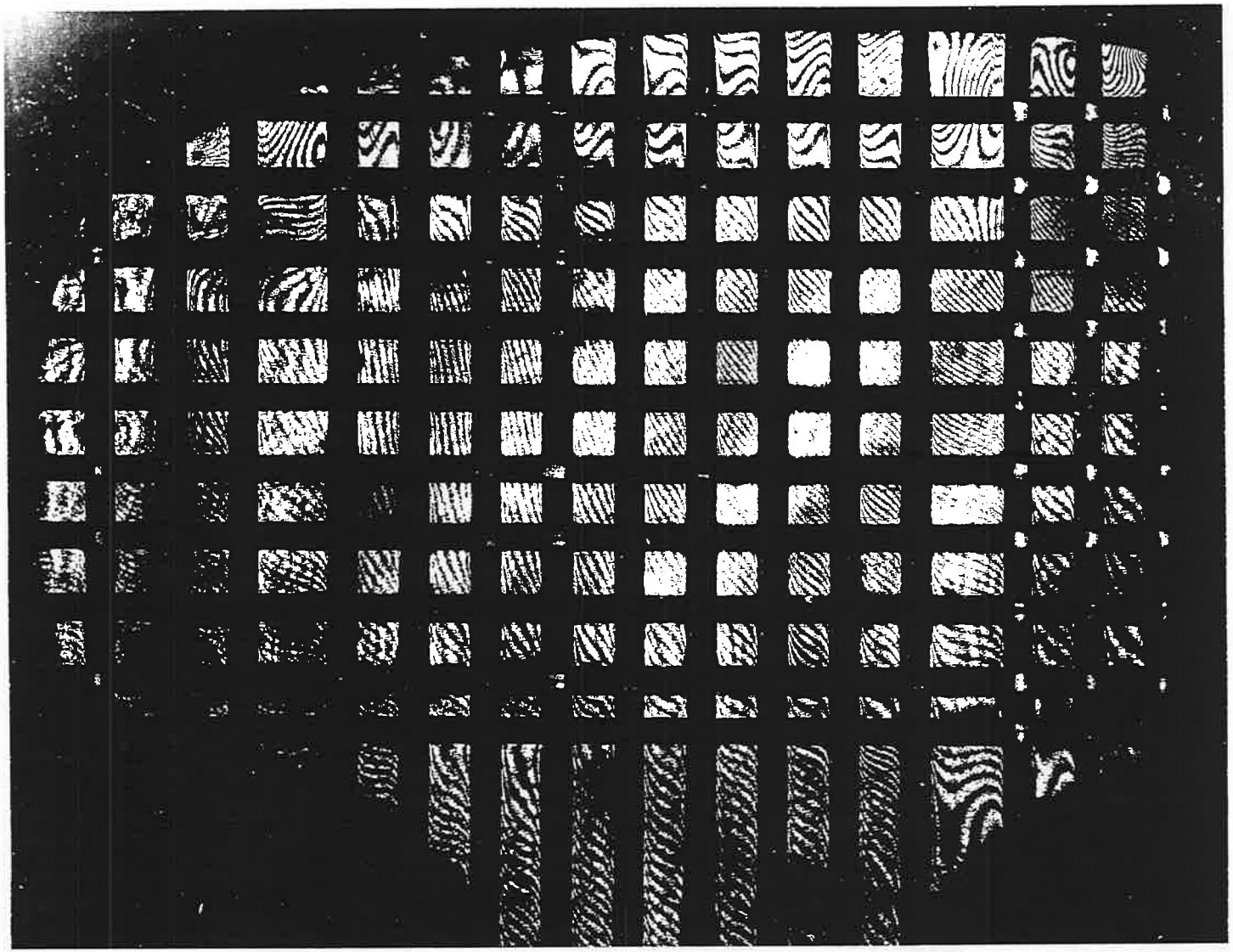

FIGURE 6a. U-FIELD FRINGE PATTERN WITH ROTATION MISMATCH FRINGES FOR THE DETERMINATION OF STRAIN SIGNS (RAIL #1, VERTICAL SLICE)

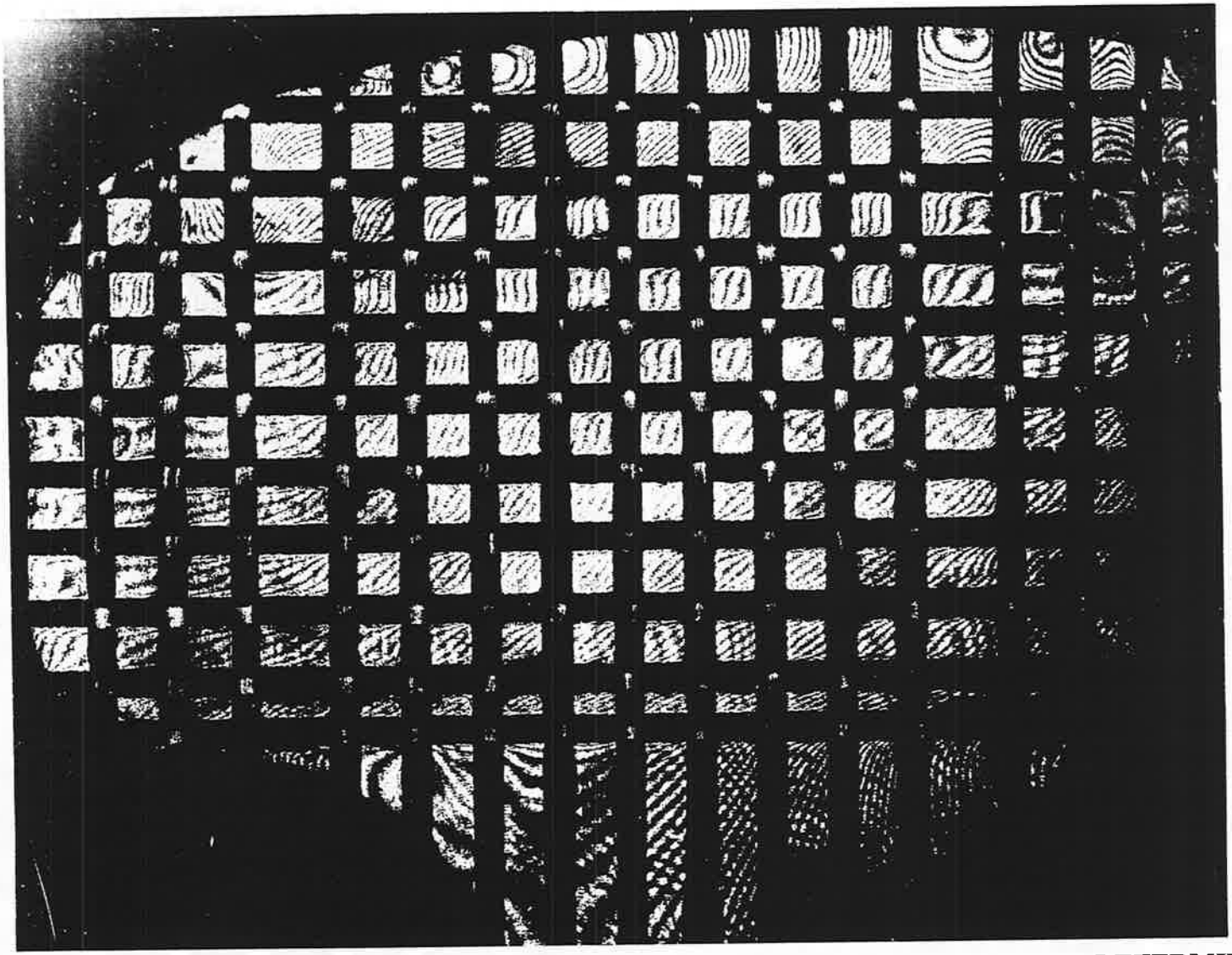

FIGURE 6b. V-FIELD FRINGE PATTERN WITH ROTATION MISMATCH FRINGES FOR THE DETERMINATION OF STRAIN SIGNS (RAIL #1, VERTICAL SLICE)

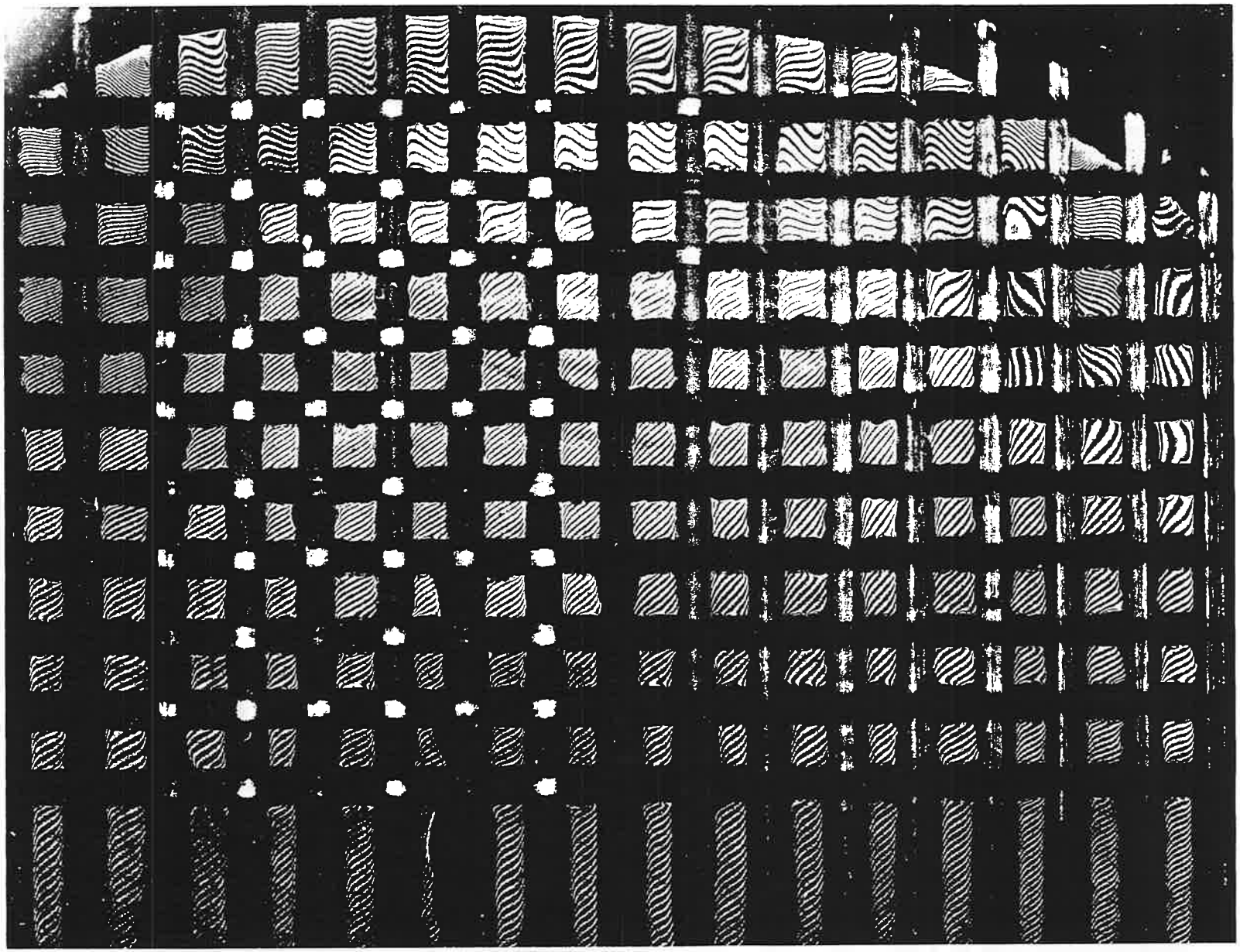

FIGURE 6c. U-FIELD FRINGE PATTERN WITH ROTATION MISMATCH FRINGES FOR THE DETERMINATION OF STRAIN SIGNS (RAIL #1, OBLIQUE SLICE)

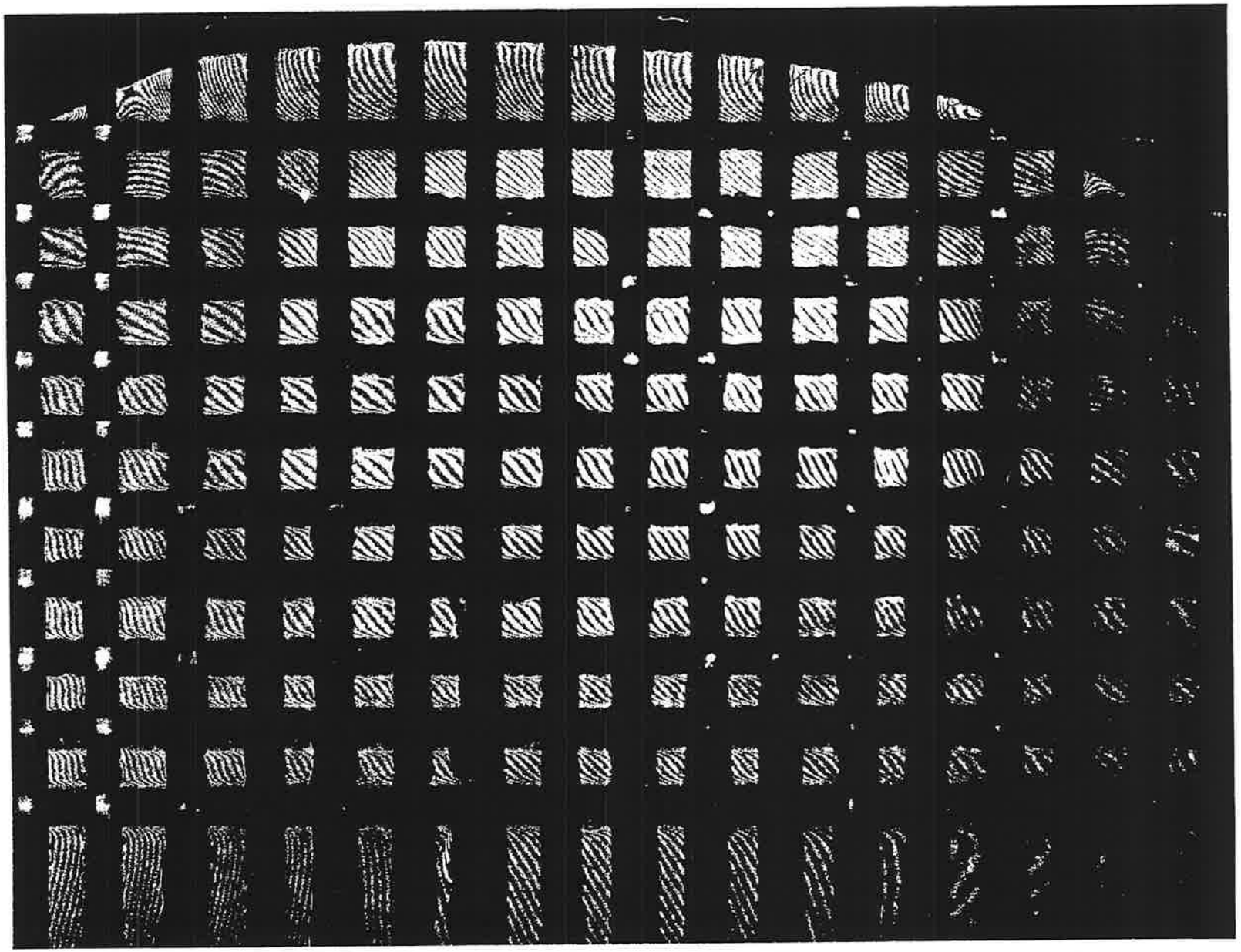

FIGURE 6d. V-FIELD FRINGE PATTERN WITH ROTATION MISMATCH FRINGES FOR THE DETERMINATION OF STRAIN SIGNS (RAIL #1, OBLIQUE SLICE)

4. ANALYSIS OF THE EXPERIMENTAL RESULTS

The strains are approximated by taking the average fringe spacings at the center of the grid elements. The strain components are calculated using,

$$\epsilon_{xx} = \frac{p}{S_{xx}} \tag{1}$$

$$\epsilon_{yy} = \frac{p}{S_{yy}} \tag{2}$$

$$\gamma_{xy} = \left(\frac{1}{S_{xy}} + \frac{1}{S_{yx}} \right) p \tag{3}$$

where p is one half of the pitch of the specimen grating, and S_{ij} $(i,j = x,y)$ are fringe spacings along x and y axes, that is, the distances between two intersected points of the fringes on the x and y axes, respectively. Since the pitch of a grating is the inverse of its frequency, p is equal to 0.417 μm for our case.

The signs of the strains are determined by the mismatch fringe patterns. According to reference [3], when a small rotation is imposed on the reference grating, the moire fringes will rotate along the same direction if the normal strain components are positive, and in the opposite direction if negative. As for the shear strain, if the crossed fringe spacing (S_{xy} or S_{yx}) becomes smaller when the reference grating is rotated, the shear strain has the same sign as the rotation; if the crossed fringe spacing becomes larger, the shear strain has the opposite sign. The rotation mismatch is easily achieved by simply rotating the specimen in our experimental set up.

In order to calculate the stress and strain components in the longitudinal direction of the rail, two assumptions are made. First, all strain components are assumed to be constant along the z direction, and the second, the z direction is assumed to be one of the principal directions. The strain components $\epsilon_{xx}, \epsilon_{yy}$ and γ_{xy} are extracted from the vertical slice, and $\epsilon_{x'x'}, \epsilon_{y'y'}$ and $\gamma_{x'y'}$ are from the oblique slice. The inclined slice is cut along the 45 degree direction from the longitudinal direction (refer previously to Figure 2). Denoting (x',y') as the coordinate system in the oblique slice, we have the following strain transformations,

$$\epsilon_{xx} = \epsilon_{x'x'} \tag{4}$$

$$\epsilon_{yy} = \frac{1}{2}(\epsilon_{y'y'} + \epsilon_{z'z'} + \gamma_{y'z'}) \tag{5}$$

$$\epsilon_{zz} = \frac{1}{2}(\epsilon_{z'z'} + \epsilon_{y'y'} - \gamma_{y'z'}) \tag{6}$$

$$\gamma_{xy} = \frac{1}{\sqrt{2}}(\gamma_{x'y'} + \gamma_{z'x'}) \tag{7}$$

$$\gamma_{zx} = \frac{1}{\sqrt{2}}(\gamma_{z'x'} + \gamma_{x'y'}) \tag{8}$$

$$\gamma_{zy} = \epsilon_{z'z'} - \epsilon_{y'y'}. \tag{9}$$

Assuming z being a principal direction we can solve for ϵ_{zz},

$$\epsilon_{zz} = 2\epsilon_{y'y'} - \epsilon_{yy}, \tag{10}$$

since γ_{zx} and γ_{zy} are zero. The contour lines of strain components thus calculated are shown in Figures 7 and 8. These strains are due to the released stresses. The stress components are calculated from the strain components by Hooke's law but an additional negative sign is imposed, because the residual stresses have the opposite sign as that of the released stresses. Figures 9 and 10 show the contours of stress components of the two rails.

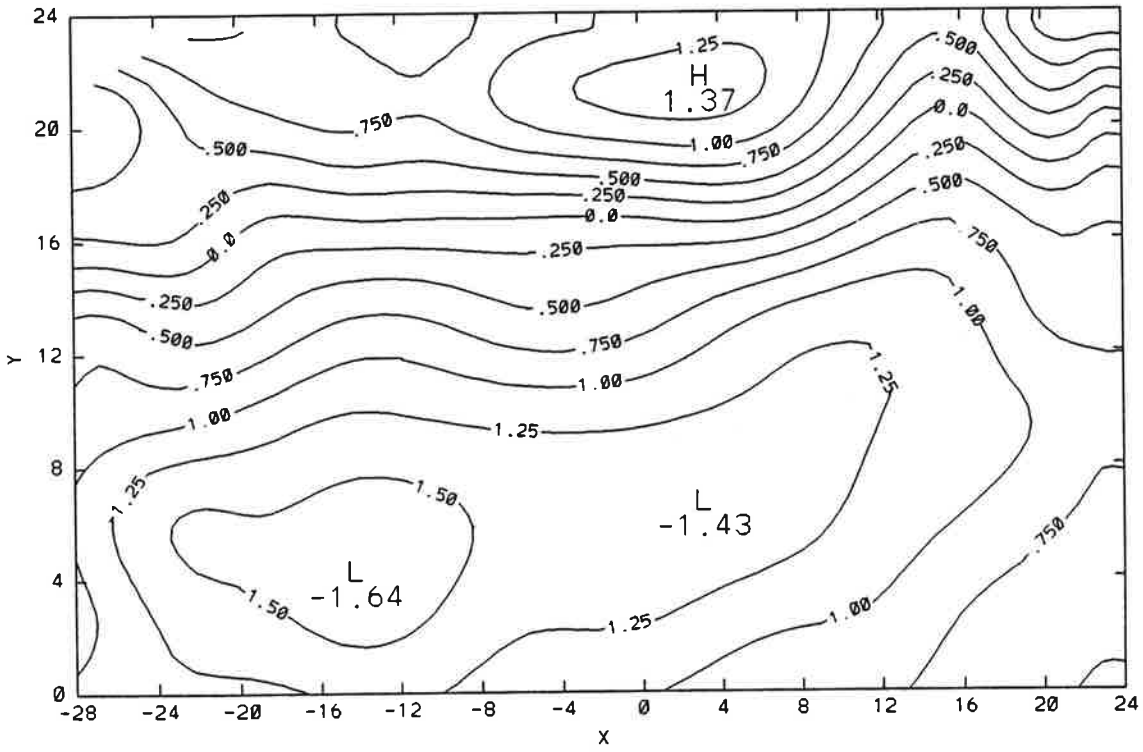

7a. Contours of ϵ_{xx} in 1000 $\mu\epsilon$

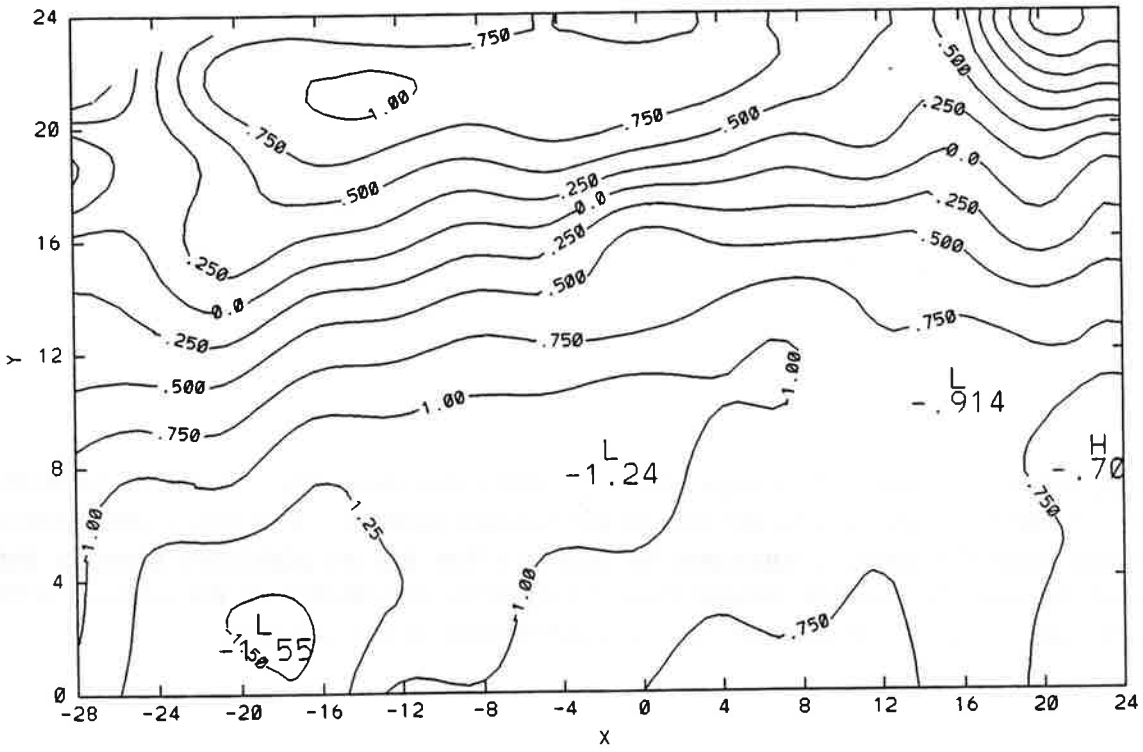

7b. Contours of $\epsilon_{x'x'}$ in 1000 $\mu\epsilon$ of the oblique slice

FIGURE 7. CONTOURS OF RELEASED STRAIN COMPONENTS OF RAIL A5

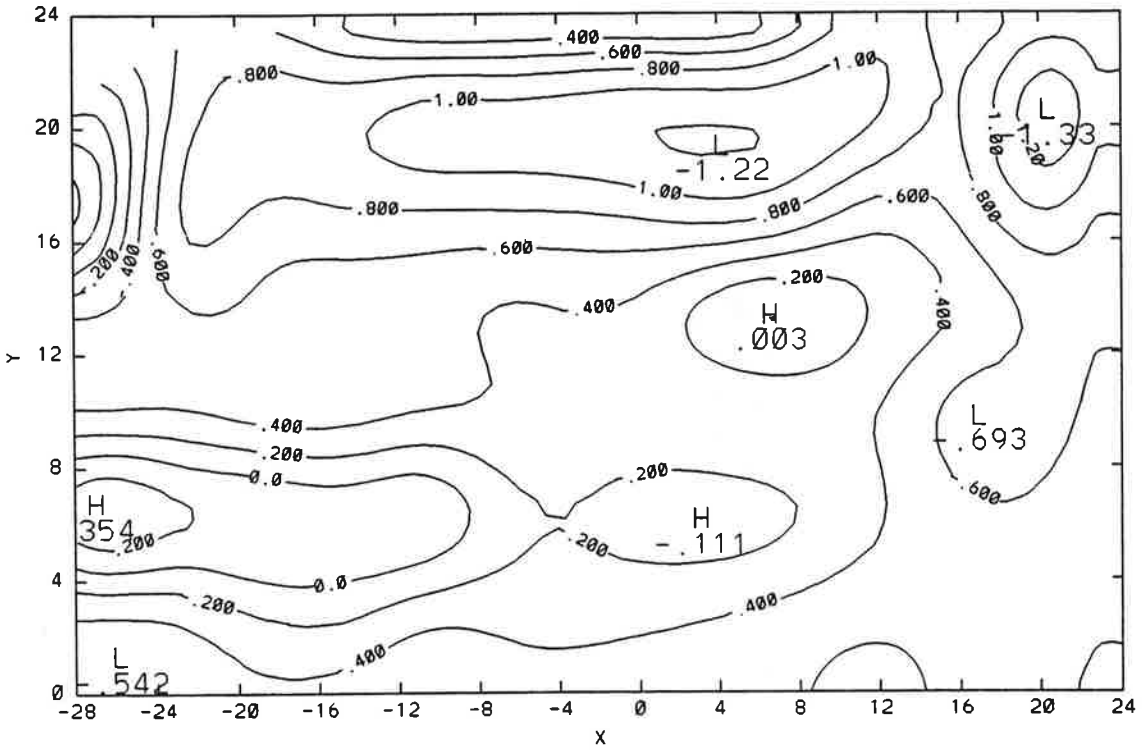

7c. Contours of ϵ_{yy} in 1000 $\mu\epsilon$

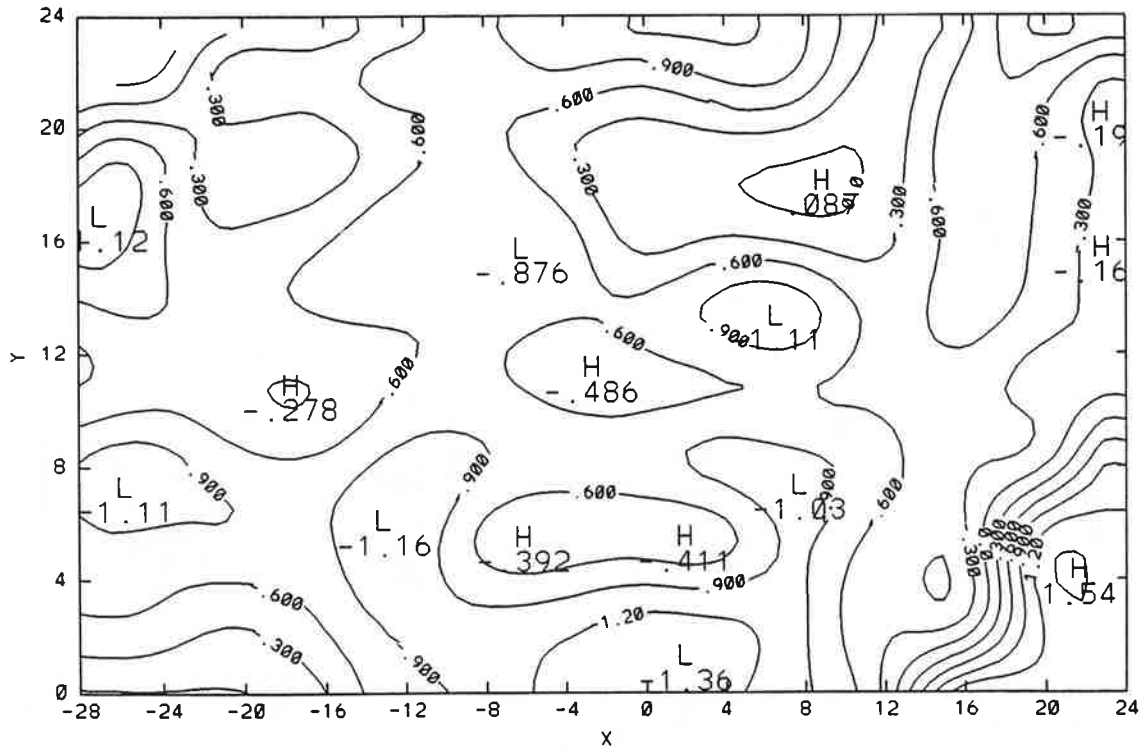

7d. Contours of ϵ_{zz} in 1000 $\mu\epsilon$

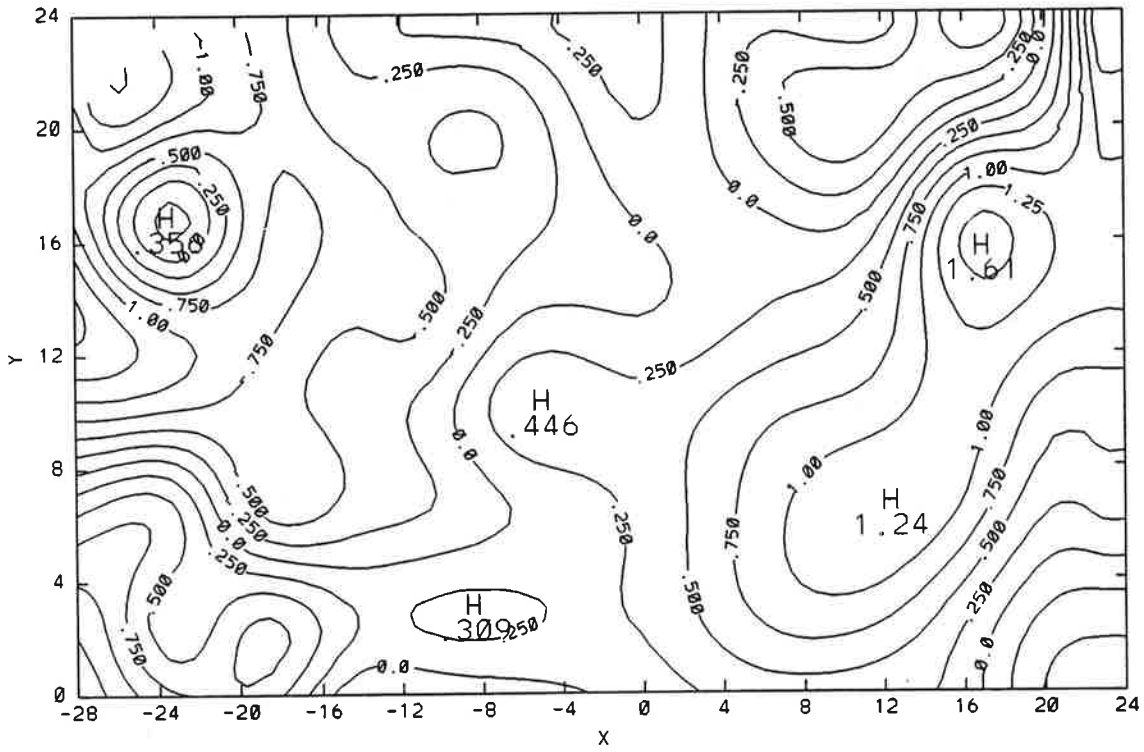

7e. Contours of γ_{xy} in 1000 $\mu\epsilon$

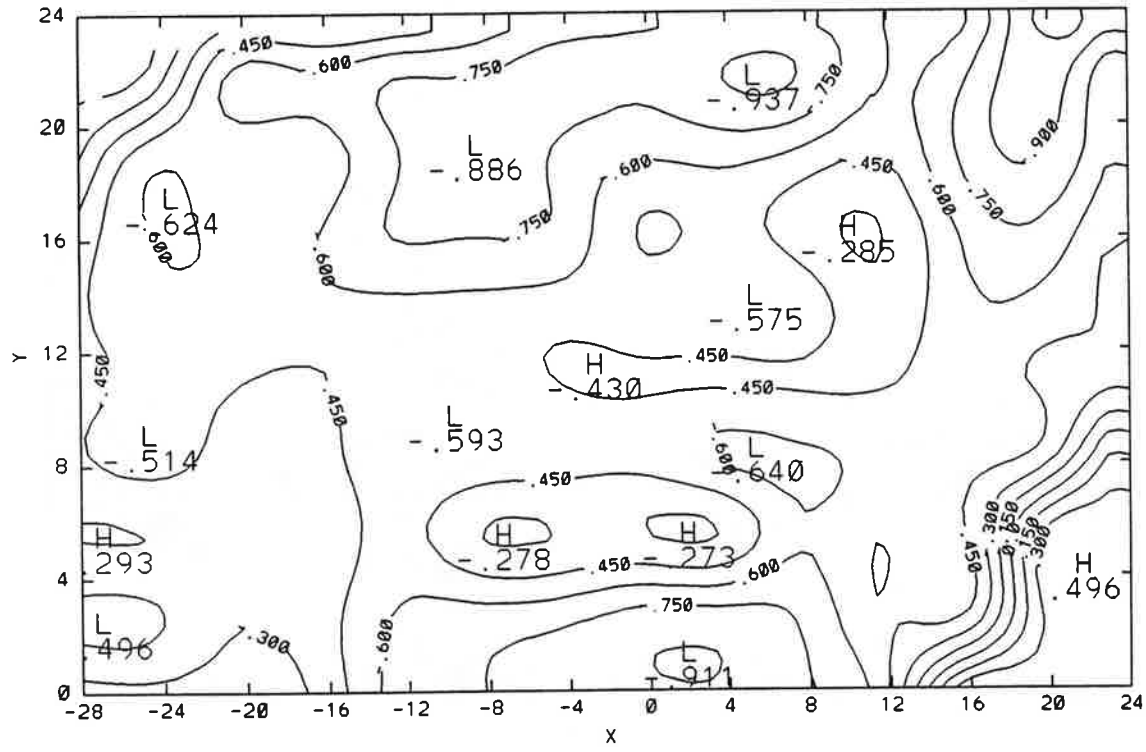

7f. Contours of $\epsilon_{y'y'}$ in 1000 $\mu\epsilon$ of the oblique slice

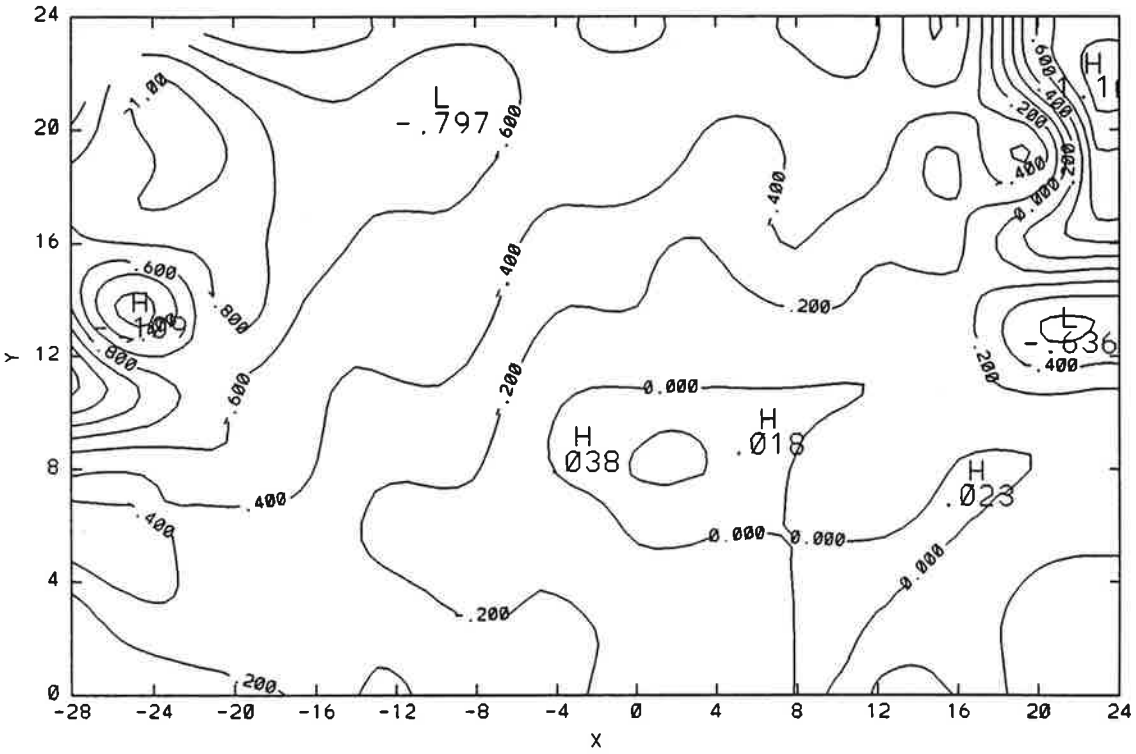

7g. Contours of $\gamma_{x'y'}$ in 1000 $\mu\epsilon$ of the oblique slice

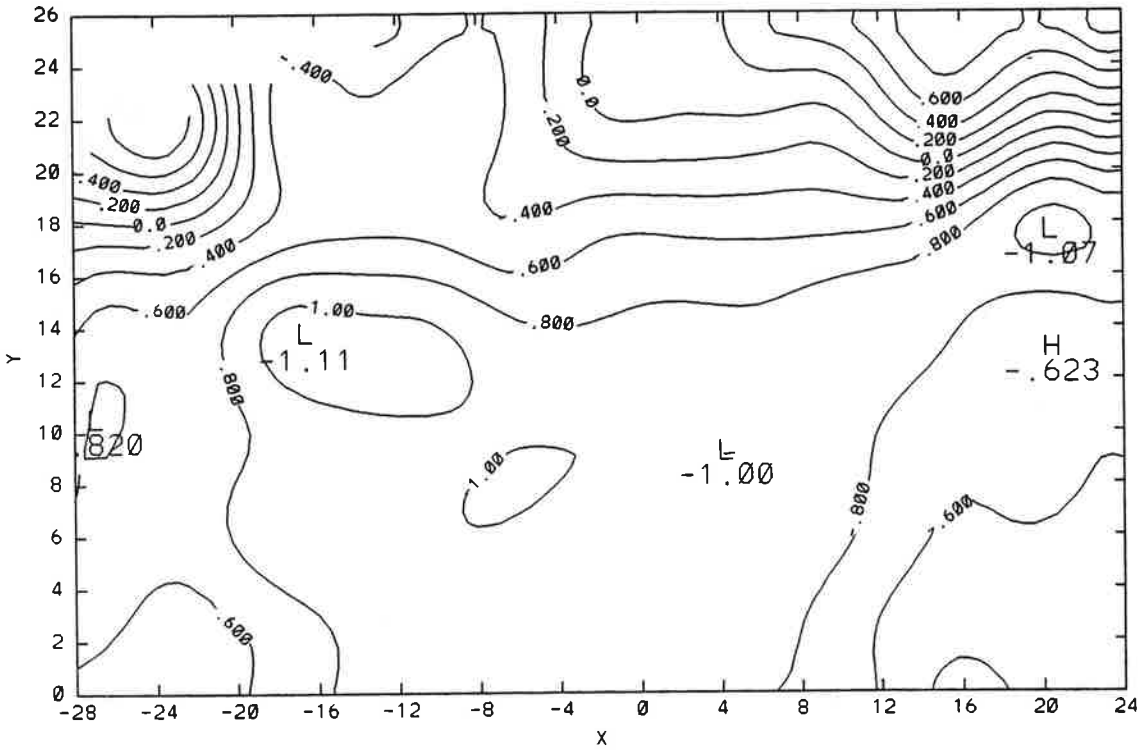

8a. Contours of ϵ_{xx} in 1000 $\mu\epsilon$

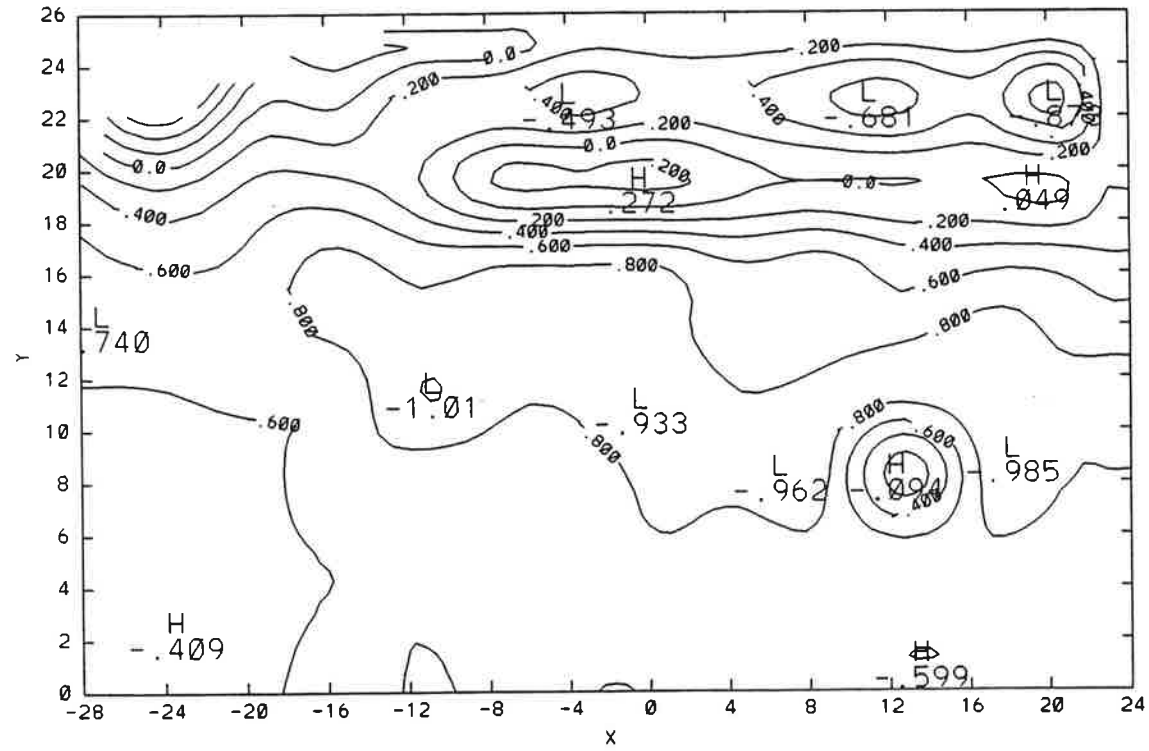

8b. Contours of $\epsilon_{x'x'}$ in 1000 $\mu\epsilon$ of the oblique slice

FIGURE 8. CONTOURS OF RELEASED STRAIN COMPONENTS OF RAIL #1

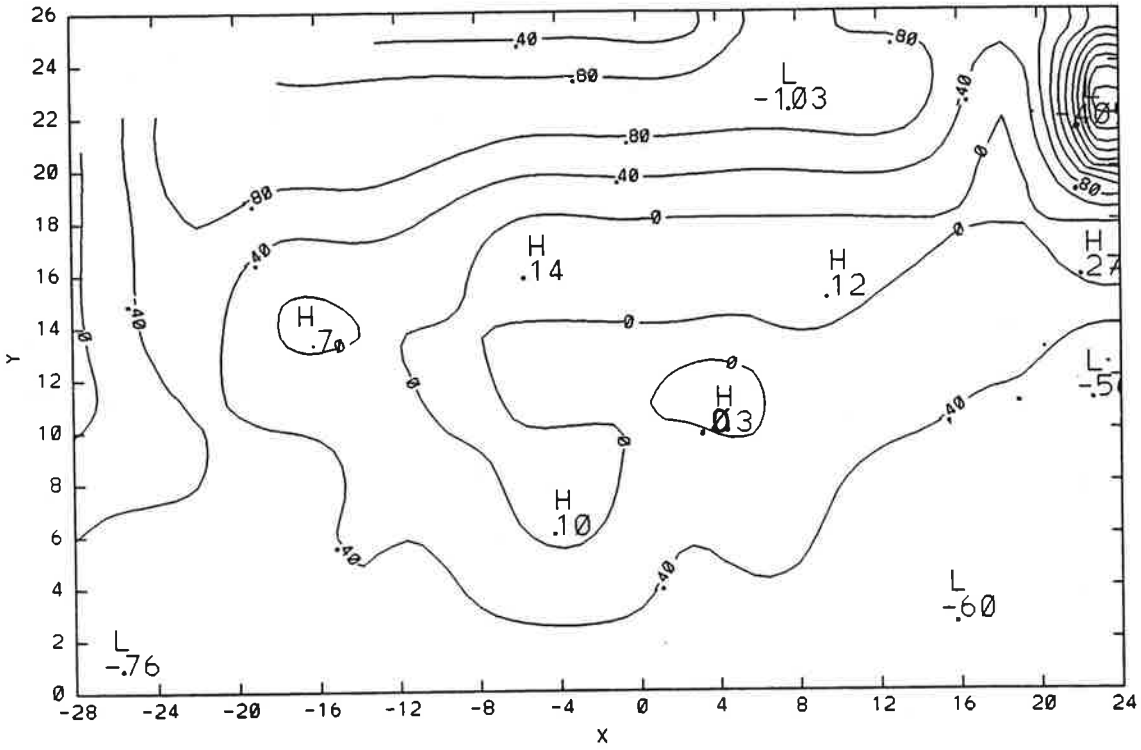

8c. Contours of ϵ_{yy} in 1000 $\mu\epsilon$

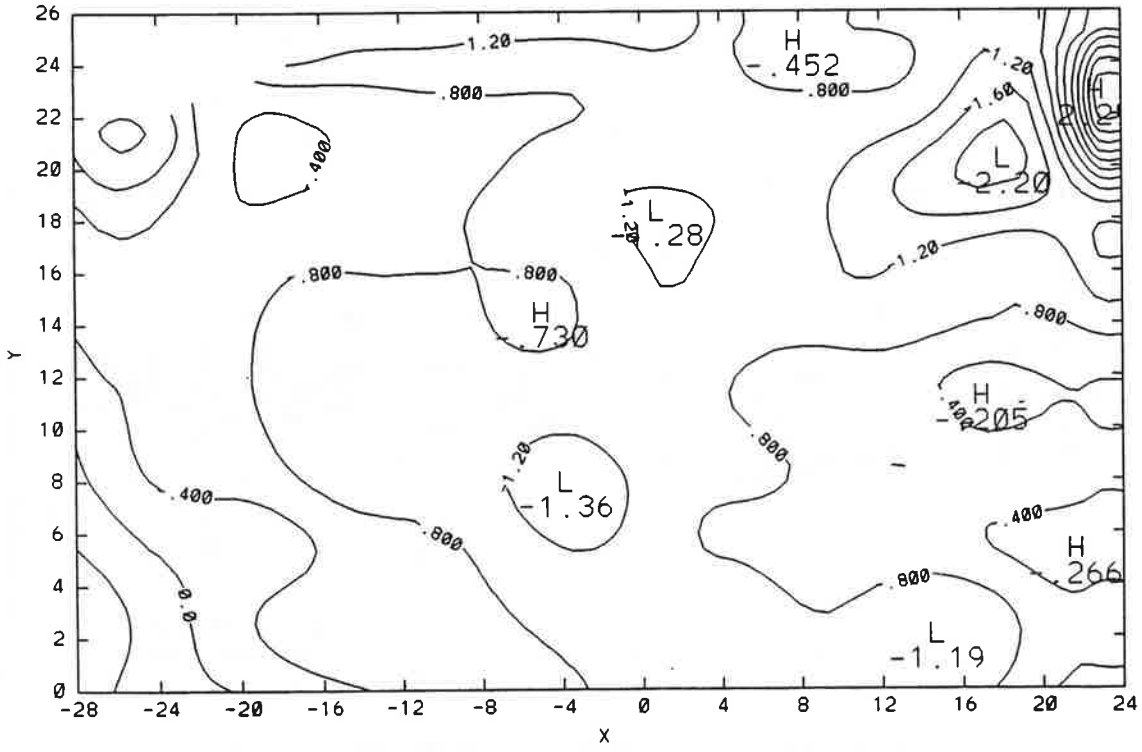

8d. Contours of ϵ_{zz} in 1000 $\mu\epsilon$

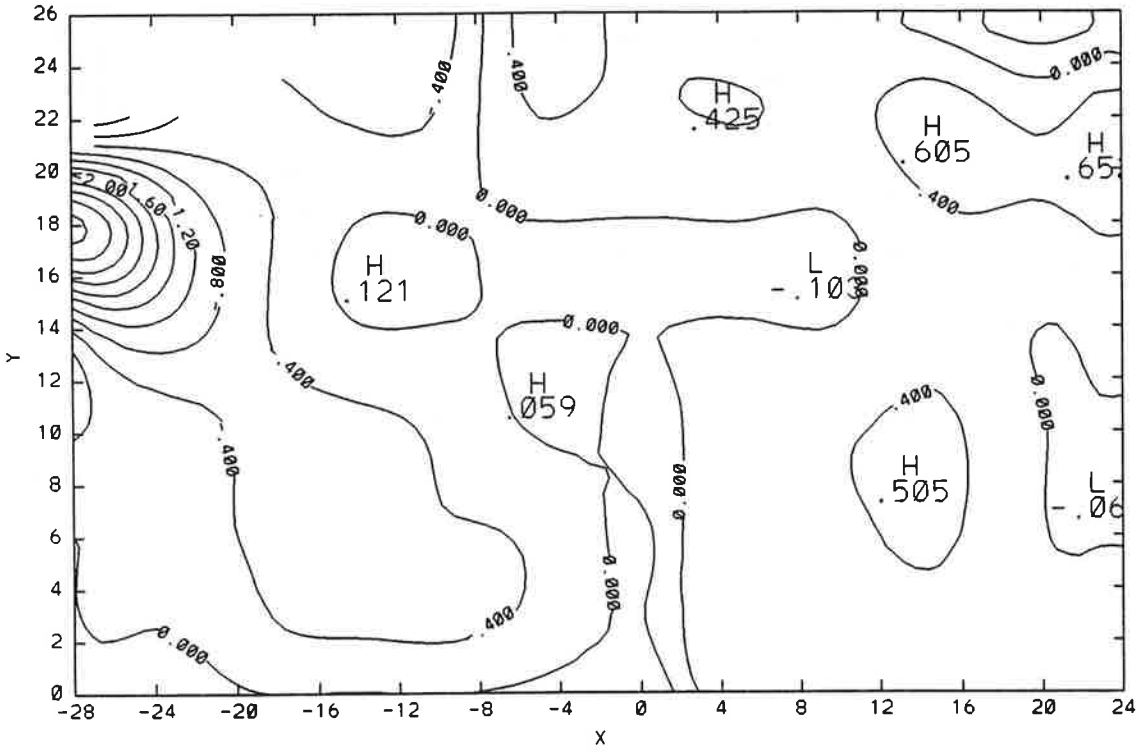

8e. Contours of γ_{xy} in 1000 $\mu\epsilon$

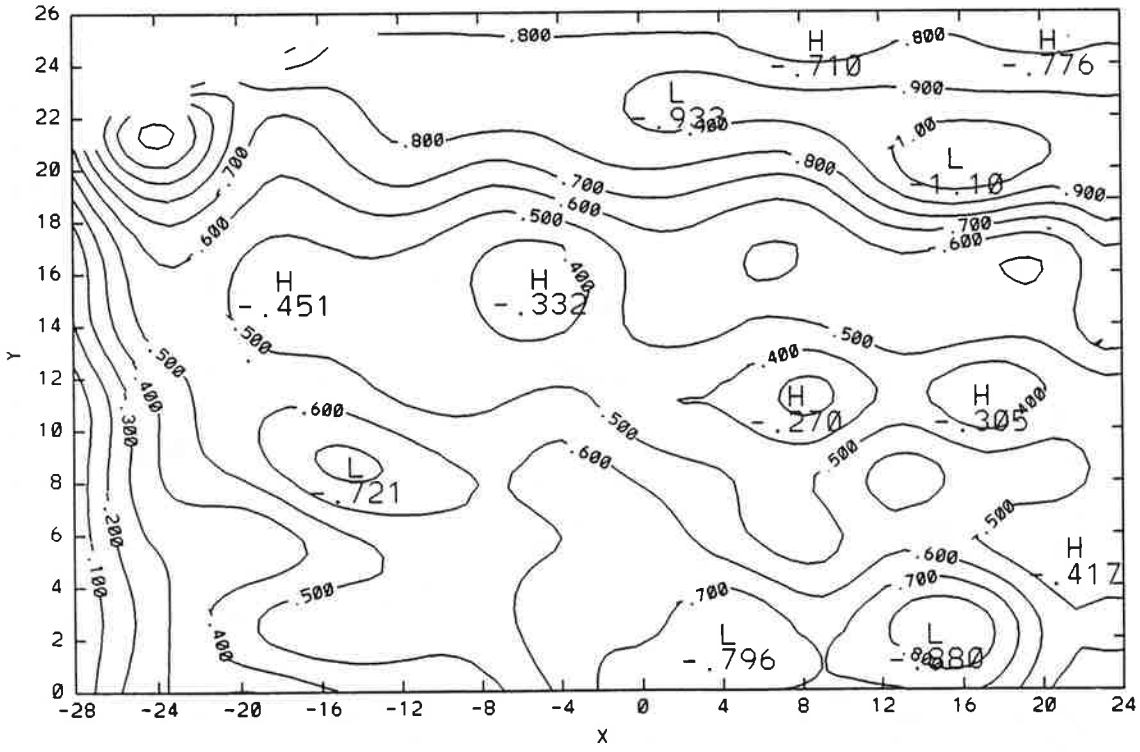

8f. Contours of $\epsilon_{y'y'}$ in 1000 $\mu\epsilon$ of the oblique slice

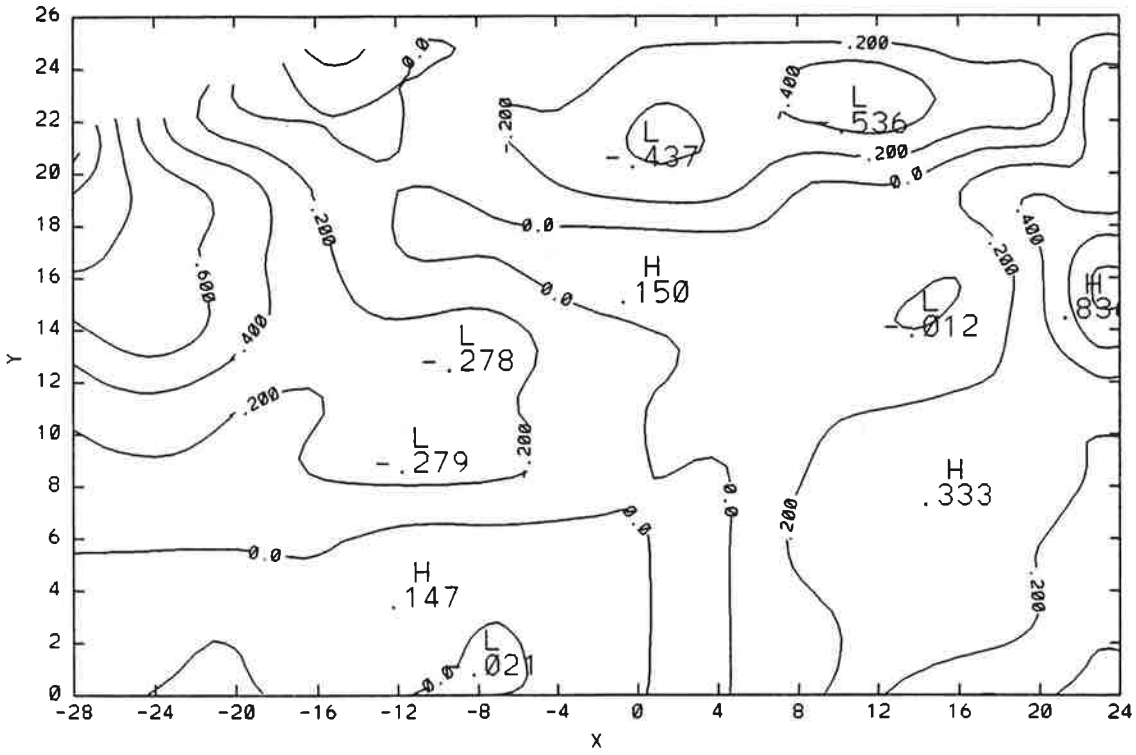

8g. Contours of $\gamma_{x'y'}$ in 1000 $\mu\epsilon$ of the oblique slice

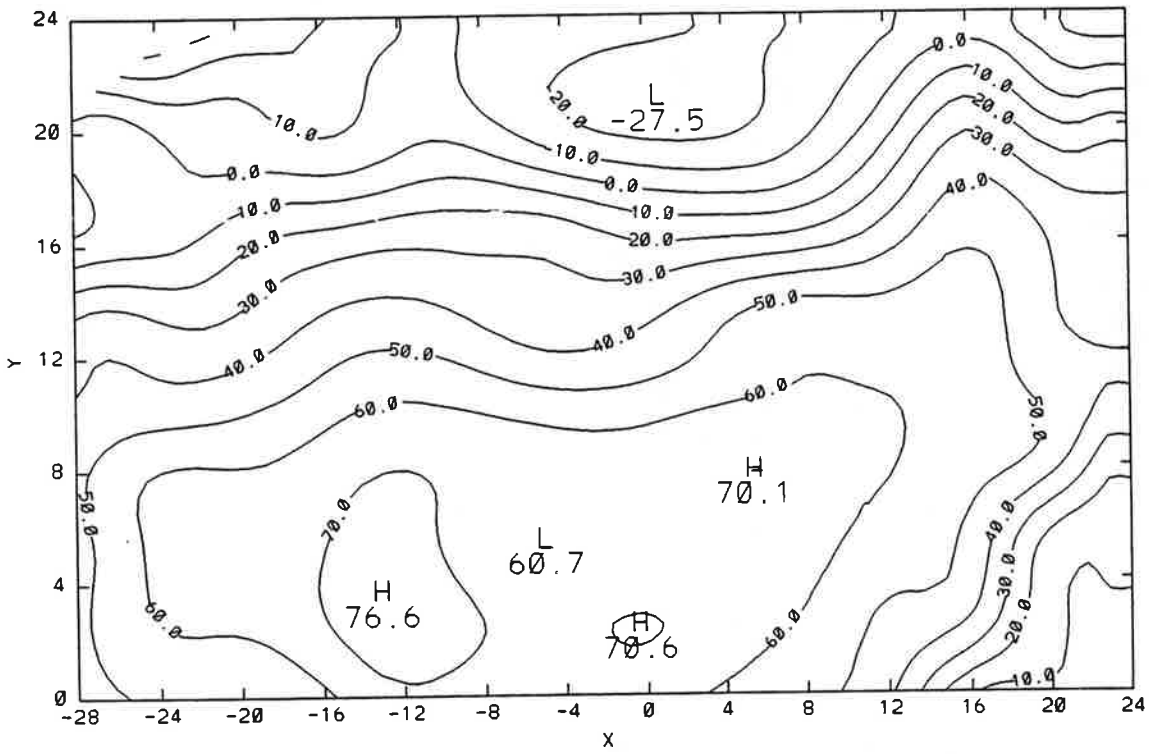

9a. Contours of σ_{xx} in KSI

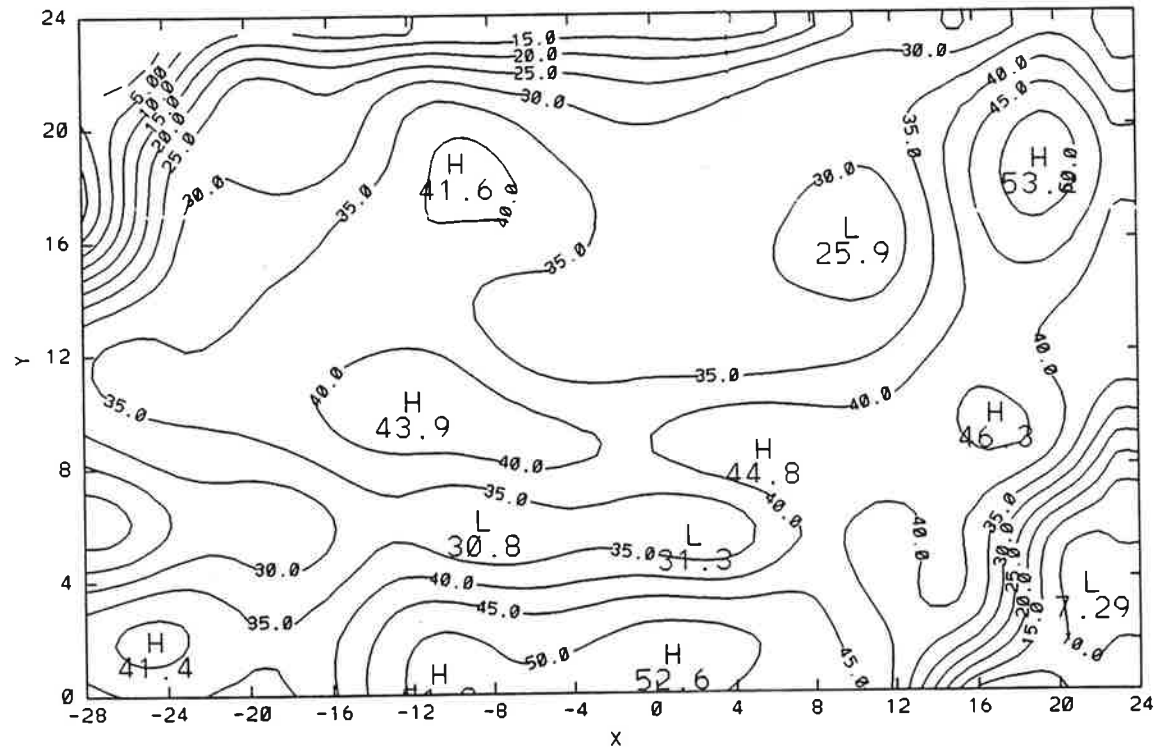

9b. Contours of σ_{yy} in KSI

FIGURE 9. CONTOURS OF RESIDUAL STRESS COMPONENTS OF RAIL A5

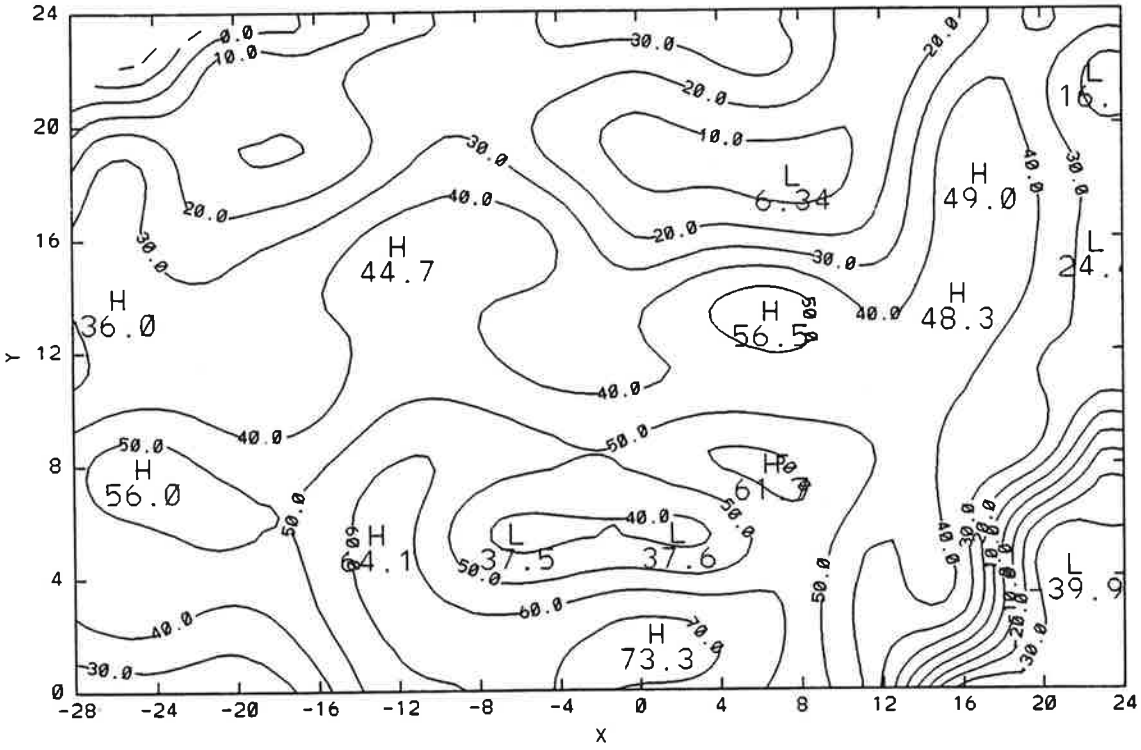

9c. Contours of σ_{zz} in KSI

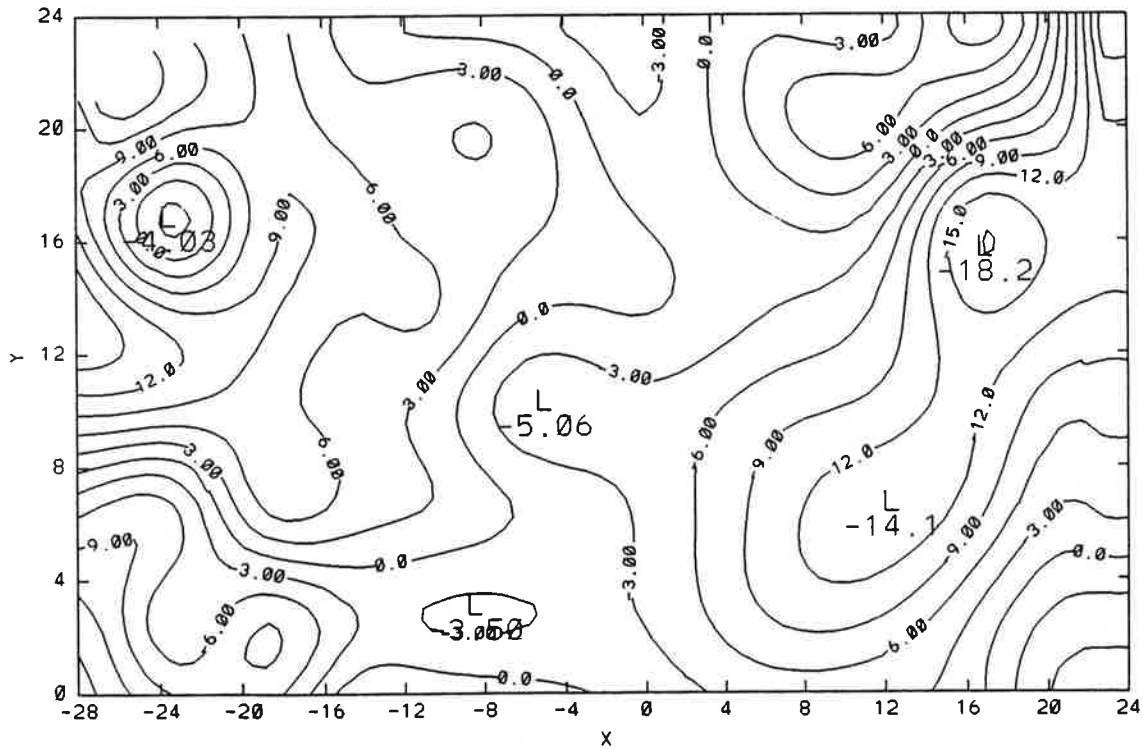

9d. Contours of τ_{xy} in KSI

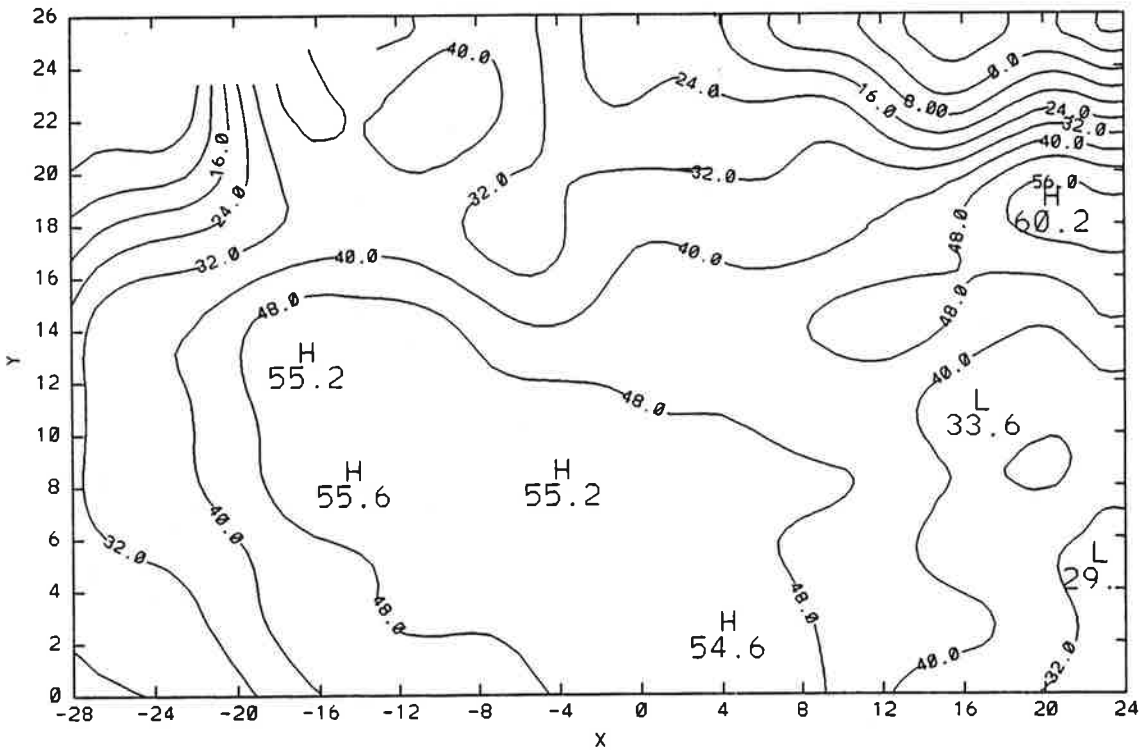

10a. Contours of σ_{xx} in KSI

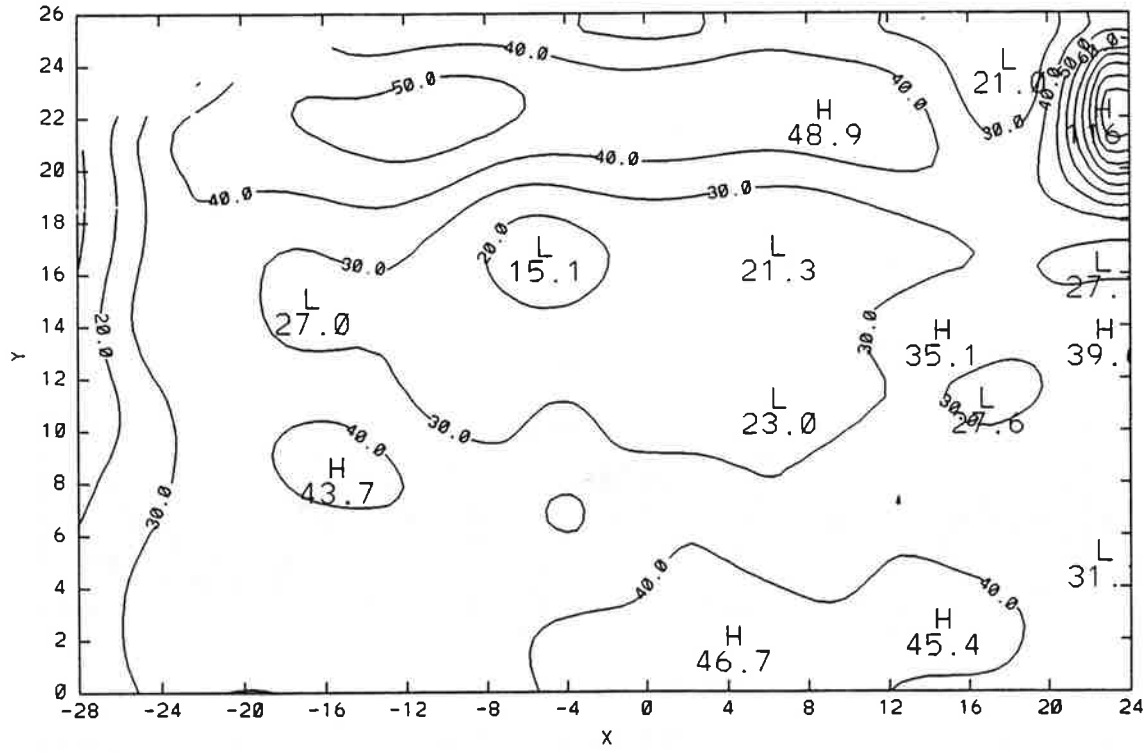

10b. Contours of σ_{yy} in KSI

FIGURE 10. CONTOURS OF RESIDUAL STRESS COMPONENTS OF RAIL #1

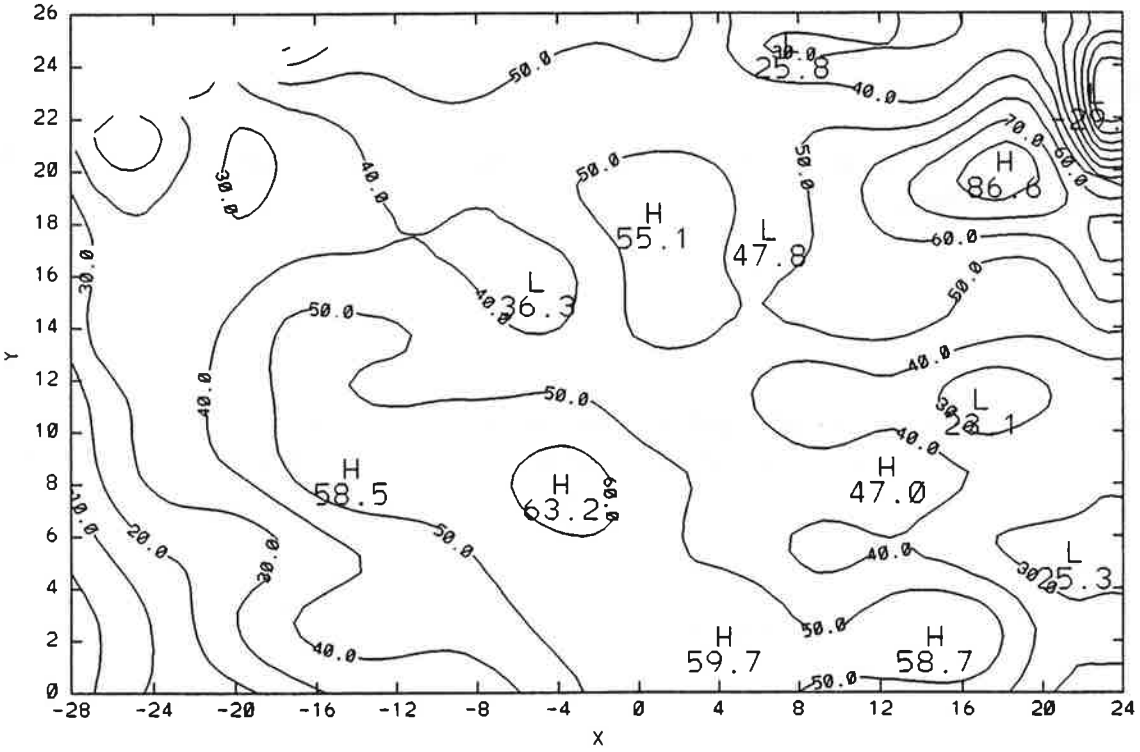

10c. Contours of σ_{zz} in KSI

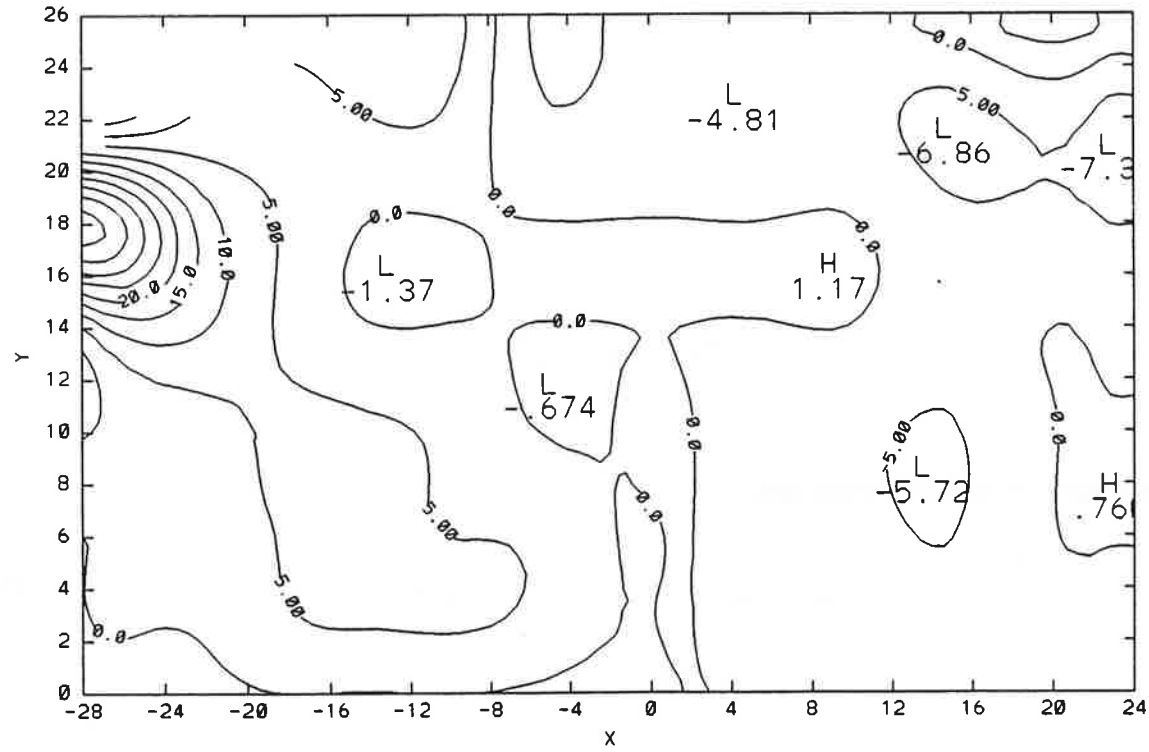

10d. Contours of τ_{xy} in KSI

4.1 Principal Stresses

It is known that the principal values of the stress deviator are the three roots of the following cubic equation [4],

$$\lambda^3 - II_s\lambda - III_s = 0 \tag{11}$$

where, λ denotes any one of the principal deviator stresses, II_s, III_s are the second and the third invariant of the stress deviator. The three independent roots of equation (11) can be expressed explicitly by,

$$\sigma_k' = 2(\cos\alpha_k)\left(\frac{II_s}{3}\right)^{\frac{1}{2}}, \qquad k = 1,2,3 \tag{12}$$

where

$$\alpha_1 = \frac{1}{3}\arccos\left[\left(\frac{III_3}{2}\right)\left(\frac{3}{II_s}\right)^{\frac{3}{2}}\right] \tag{13}$$

$$\alpha_2 = \alpha_1 + \frac{2}{3}\pi \tag{14}$$

$$\alpha_3 = \alpha_1 - \frac{2}{3}\pi \tag{15}$$

Then the three principal stresses are,

$$\sigma_k = \sigma_k' + \sigma\ , \qquad k = 1,2,3 \tag{16}$$

where σ is the spherical stress tensor, i.e.,

$$\sigma = \frac{1}{3}(\sigma_{xx} + \sigma_{yy} + \sigma_{zz}). \tag{17}$$

Figures 11 and 12 show the contours of the principal stresses. A convention is taken such that the three principal stresses are in a sequence of $\sigma_1 > \sigma_2 > \sigma_3$.

4.2 Principal Directions

The secondary principal directions in the x-y plane are first determined since the z direction is assumed to be a principal direction. The angle between the maximum secondary principal direction and the x-axis is,

$$\theta_1 = \frac{1}{2} \arctan \frac{2\tau_{xy}}{\sigma_{xx} - \sigma_{yy}}. \tag{18}$$

The secondary principal stresses are then obtained by transforming the σ_{xx}, σ_{yy} and τ_{xy} onto the secondary principal directions. A comparison is made among the two secondary principal stresses and σ_{zz}. If σ_{zz} is the largest stress, it would be the maximum principal stress, otherwise, the maximum secondary principal stress would be the maximum principal stress. The angle between the maximum principal direction and x-axis is mapped in Figures 13 and 14. Figures 13a and 14a are the distributions of those points whose maximum principal stress direction are coincident with the z axis.

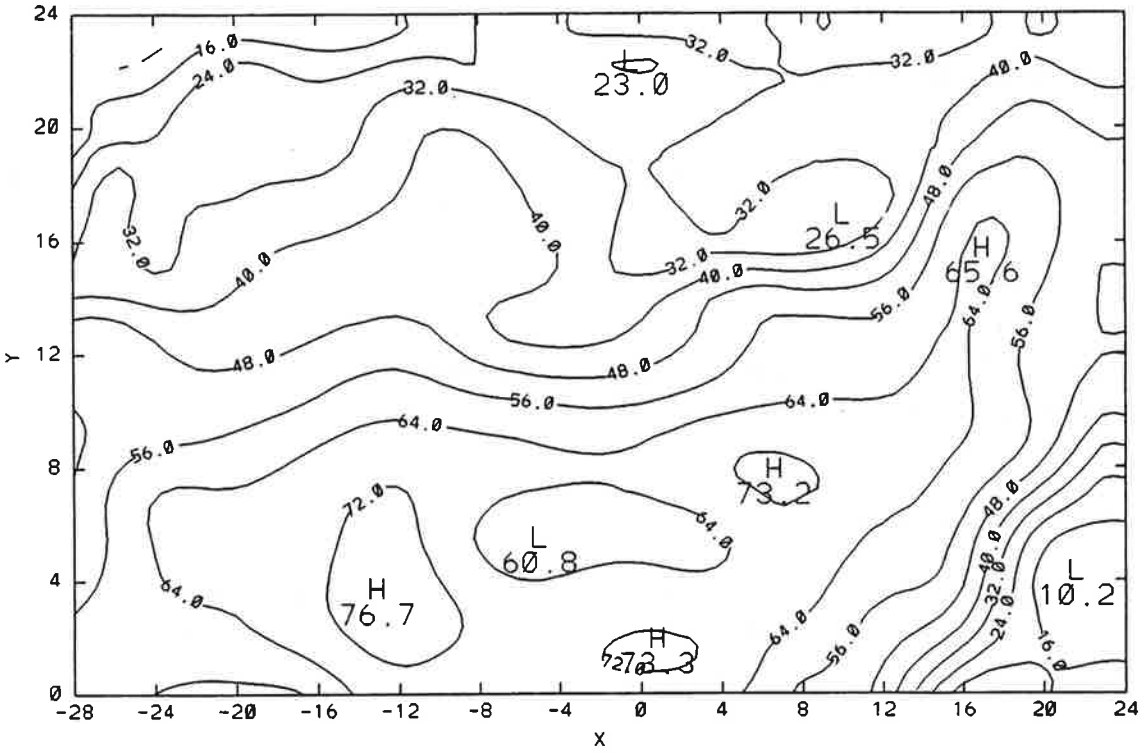

11a. Contours of σ_1 in KSI

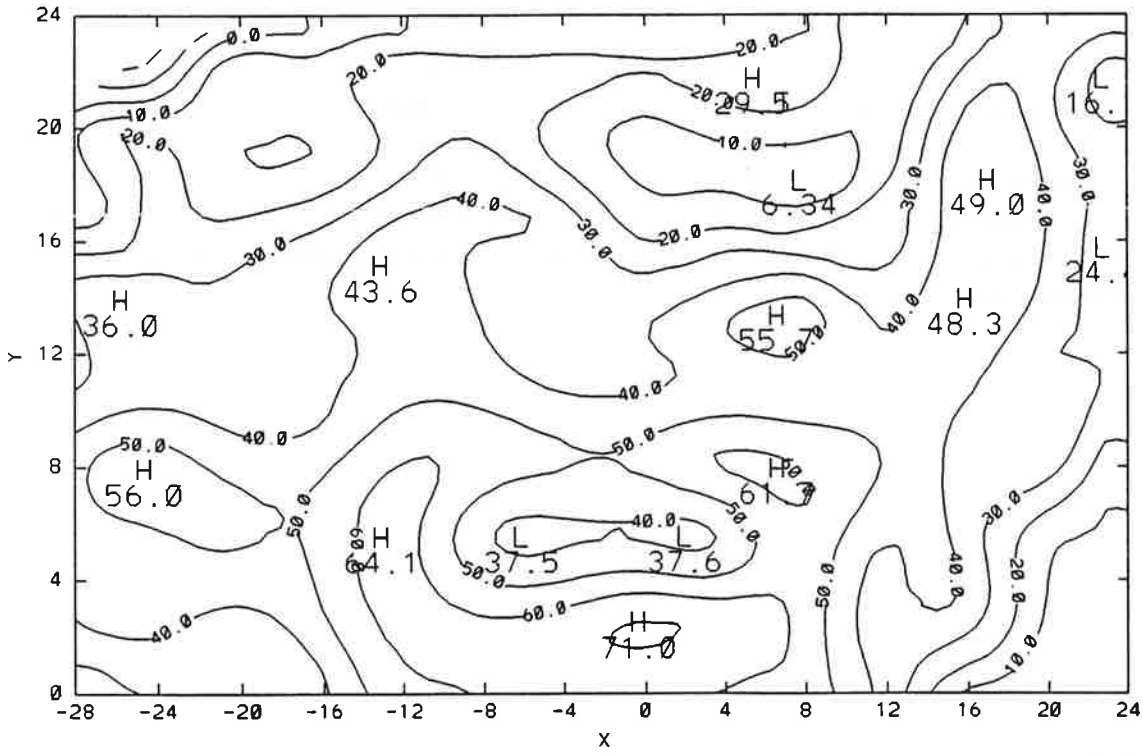

11b. Contours of σ_2 in KSI

11. CONTOURS OF THE PRINCIPAL STRESS OF RAIL A5

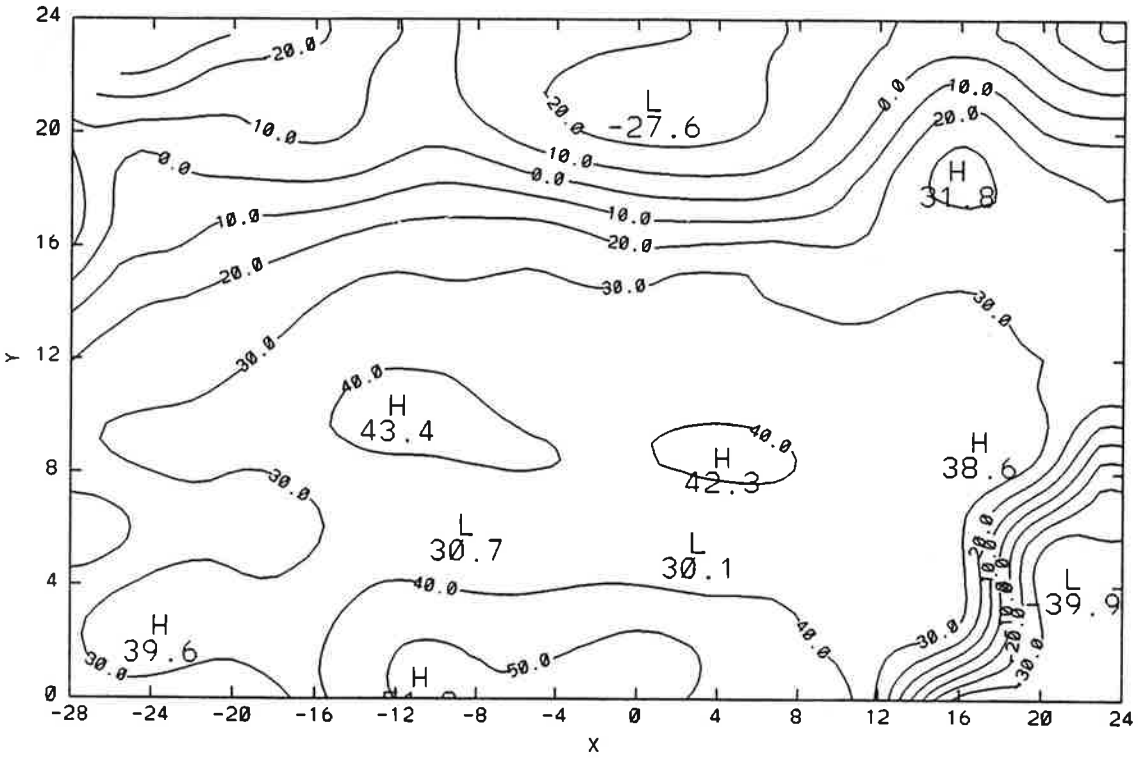

11c. Contours of σ_3 in KSI

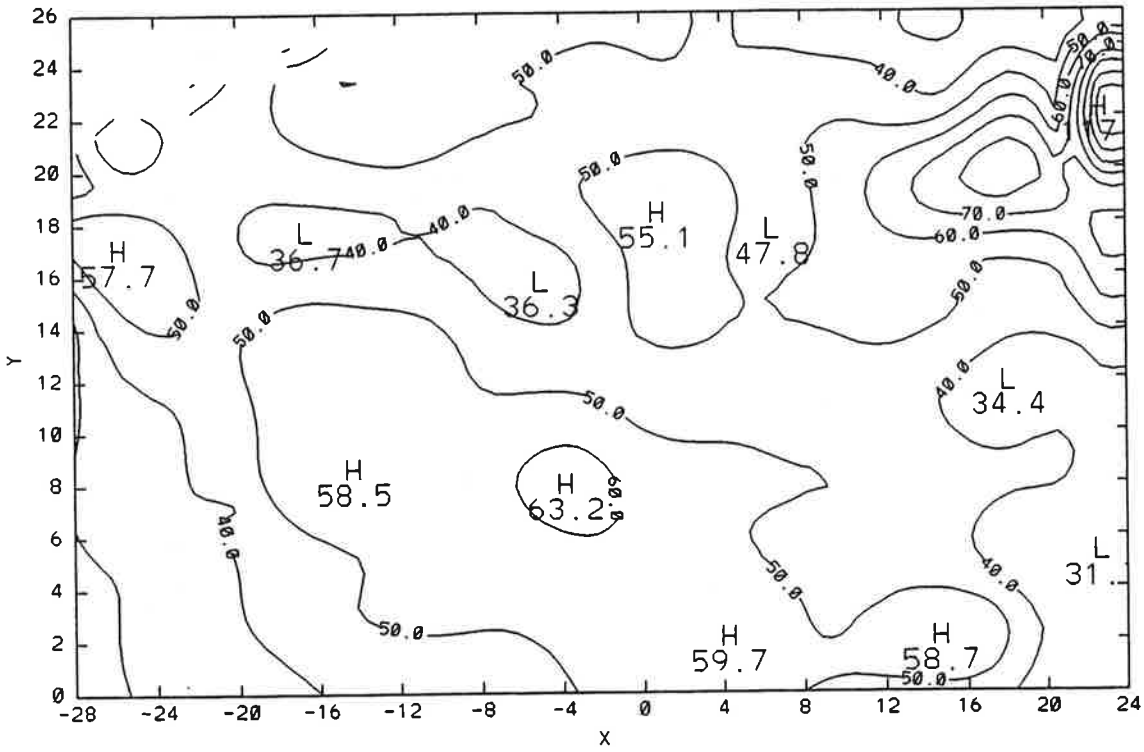

12a. Contours of σ_1 in KSI

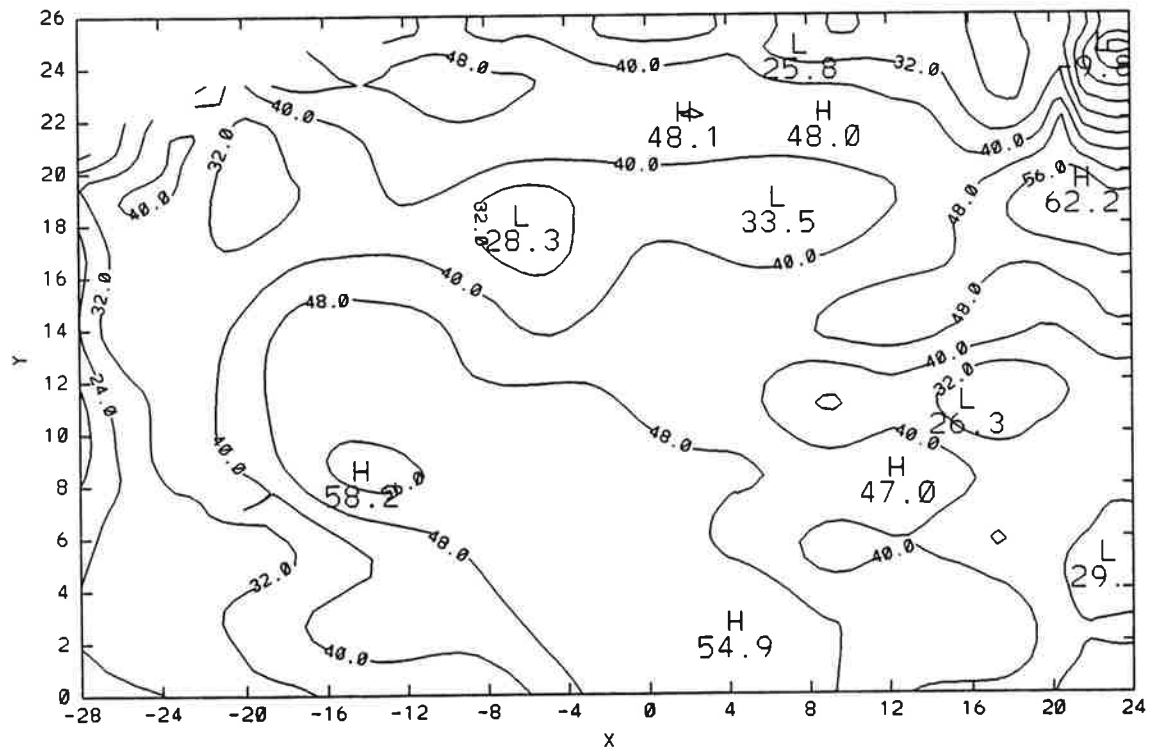

12b. Contours of σ_2 in KSI

FIGURE 12. CONTOURS OF THE PRINCIPAL STRESS OF RAIL #1

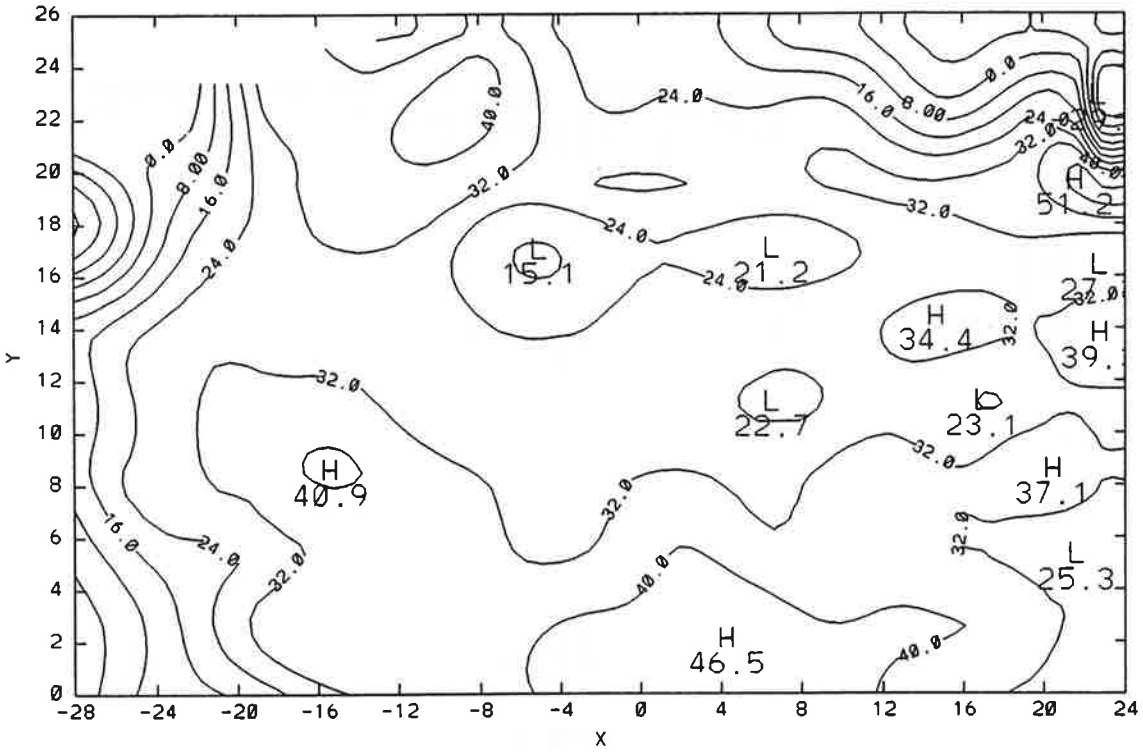

12c. Contours of σ_3 in KSI

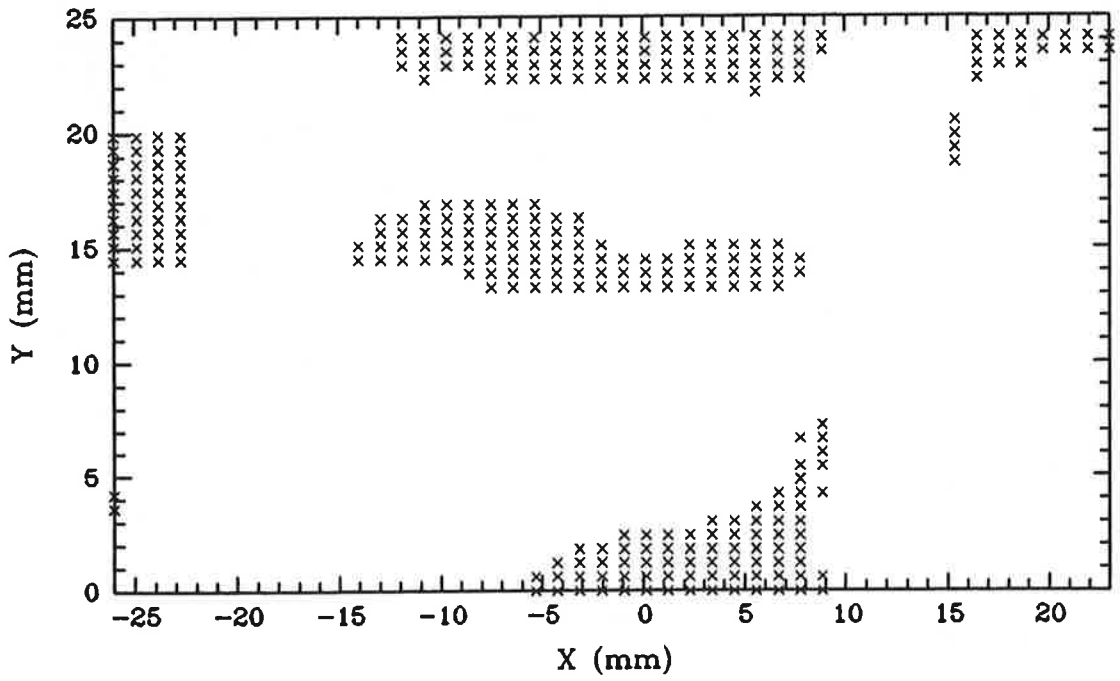

a. The distribution of σ_1 with direction in z-axis

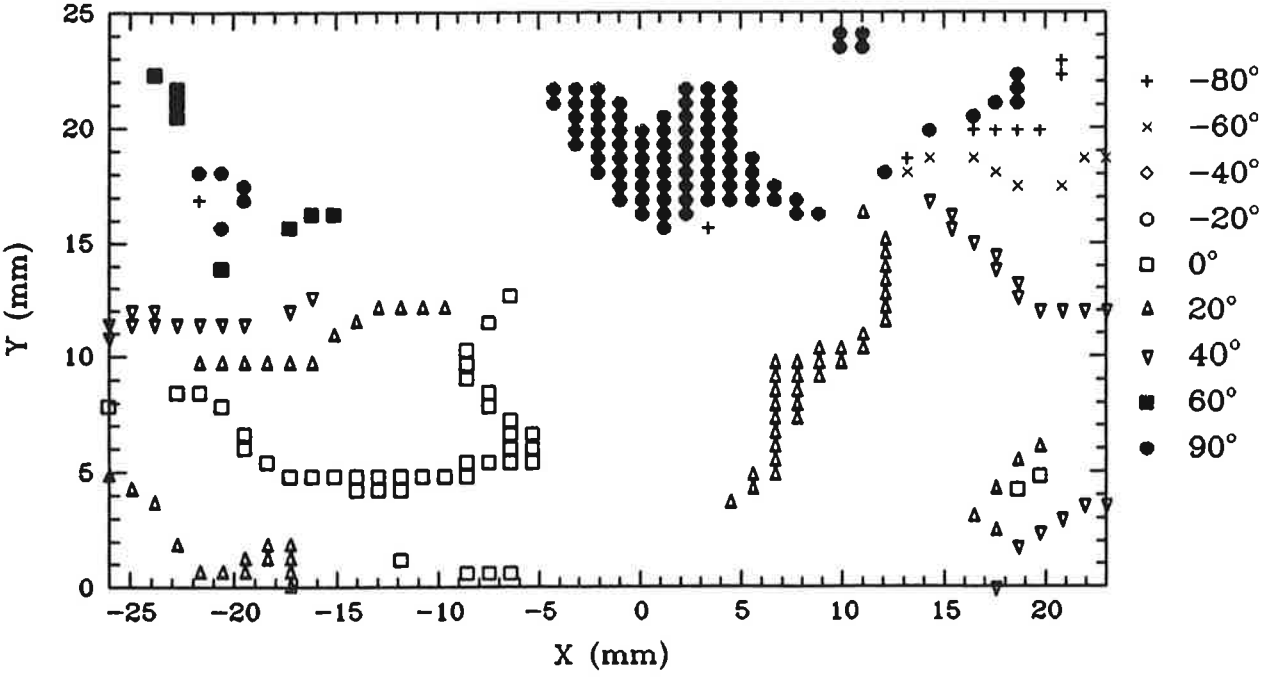

b. Distribution of σ_1 with direction in x-y plane (error band $\pm 1.5°$)

FIGURE 13. THE DIRECTION OF THE MAXIMUM PRINCIPAL STRESS OF RAIL A5

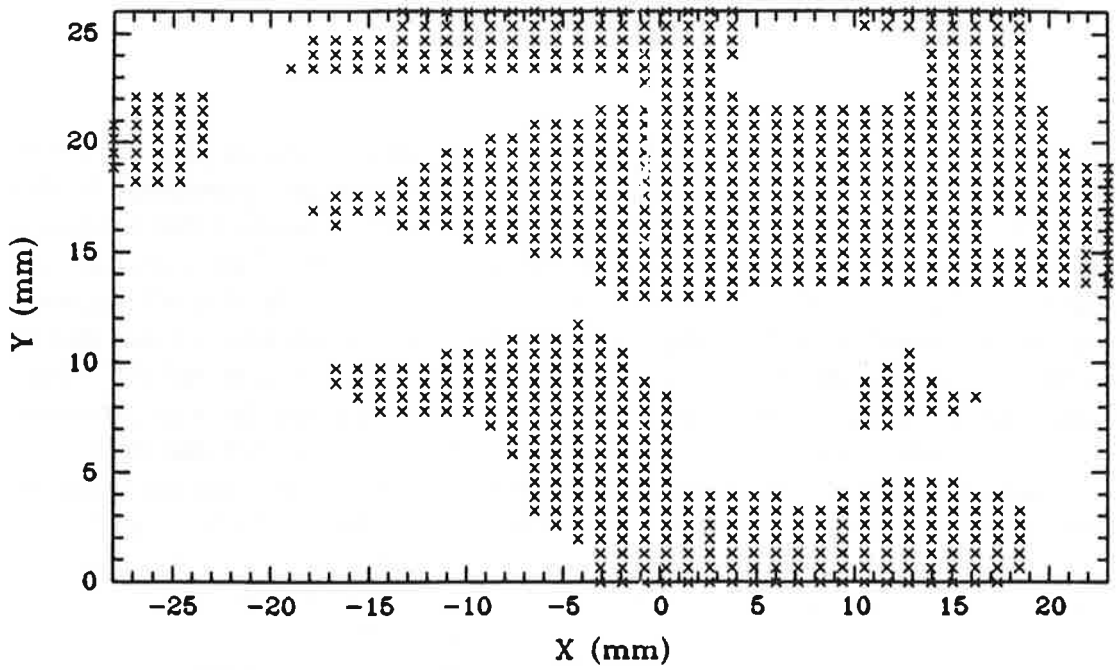

a. The distribution of σ_1 with direction in z-axis

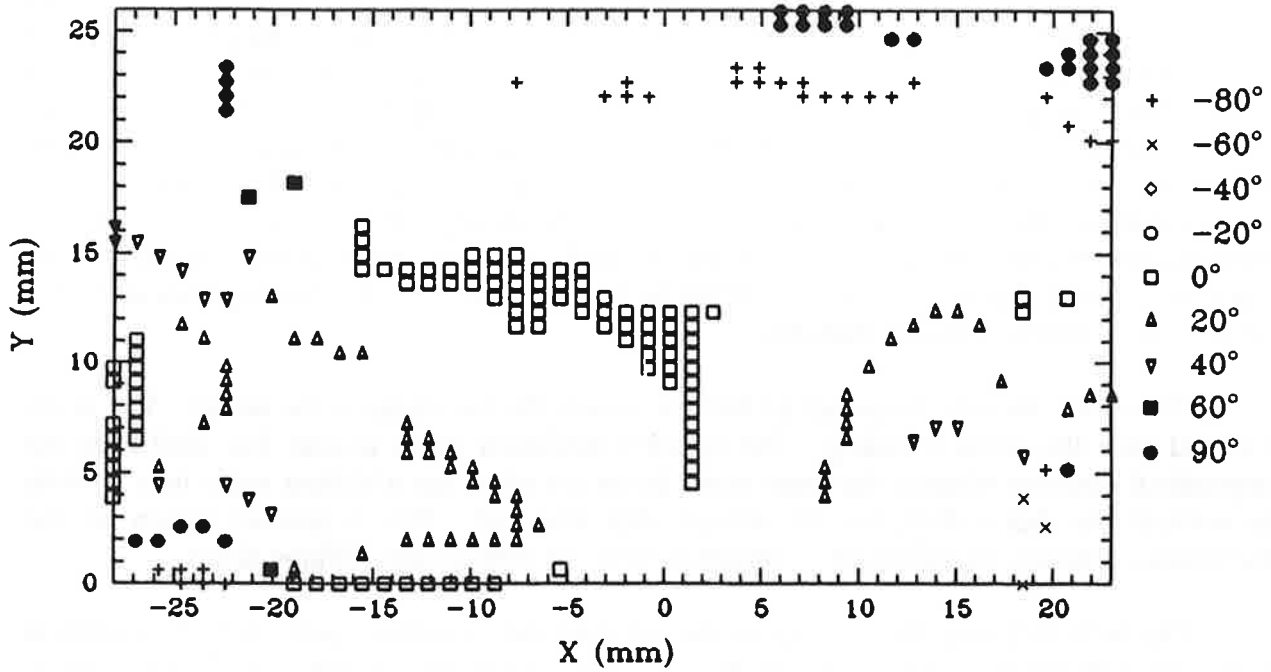

b. Distribution of σ_1 with direction in x-y plane (error band $\pm 1.5°$)

FIGURE 14. THE DIRECTION OF THE MAXIMUM PRINCIPAL STRESS OF RAIL #1

5. DISCUSSION

The study reported here is an extension of the work reported in reference [2]. Compared to the specimen in Reference 2, the area covered by moire is much larger (approximately 50 x 30 *mm* vs. 24 x 30 *mm*) and the grid element from which the average strain value is taken is smaller. The number of stress released grids is increased from 49 to 150. Two slices cut from the same rail at two different angles are analyzed. All the components of the three-dimensional stress tensor are solved based on two assumptions. The first assumption which states that all strain components are independent of z coordinate is validated by the result of rail A5. Since the inclined angle for the oblique slice is between z,y and z',y' axes and the x axis remains unchanged, the strain component ϵ_{xx} must be the same for both the vertical slice and the oblique slice when y' is projected onto y. And the experimental results show that there are sufficient similarities between ϵ_{xx} of the vertical slice and that of the oblique slice (refer back to Figures 7a and 7b) taking into account the fair amount of the experimental error due to the averaging process with each grid element. It should be noted that the y axis of the oblique slice is the projected value in Figure 7b. The stress components are obtained from the strain components of both slices, they are not inspected for the two slices individually. In other words, the stress components of one point have to be calculated from the strain components of the corresponding points of the two slices.

However, the story of the other rail is different. One could not say that the distribution of ϵ_{xx} is the same for the vertical slice and for the oblique slice of this rail (refer back to Figures 8a and 8b). It is believed that the machining stress introduced by the cutting process is much larger for the oblique slice of this rail than that of rail A5. This is because the thickness of this oblique slice is only 0.25 inches. During the cutting process the specimen is held on the grinder by a magnet table. For a thin slice, the magnet field intrudes into the surface of the slice and magnetizes the cutting chips. As a result, the magnetized chips could not be sucked by the vacuum and accumulated quickly around the ends of the cutting grooves. The ventilation was disrupted and the heat generated by cutting resulted in machining stresses. Based on our experiences, the thickness of a slice should not be less than half an inch. The experimental error for this rail is therefore larger than that for rail A5.

There is a shell at the corner of Rail #1, where the rail contacts the wheel. The crack is closed after the stress releasing. The detected maximum stress around this shell is in the longitudinal direction whereas the shear stress in the x-y plane has a highest value here. While the vertical slice has a shell, but the oblique slice does not. This is another reason for the discrepancy between the values of ϵ_{xx} obtained from the vertical and oblique slices.

For both rails near the top edge of the rail head the maximum principal stress tends to be aligned with the longitudinal axis of the rail (refer to Figures 13 and 14). The maximum stress values are generally the same for the two rails except that the first principal stress reaches as high as 117 KSI at one corner of rail #1 (see Figure 12a). This high stress is in the y direction. One assumption taken in this analysis is that the z axis is one principal direction.

This means that the stress component σ_z is one principal stress but not necessarily σ_3. It can be seen from Figure 13a and 14a that the maximum principal stress, *i.e.*, σ_1, of large portion of the rail section is in the z direction.

The dissection technique adopted here can give only the average strain value at the center of one grid element. It may also involve more or less machining stresses during the grid cutting process. In addition, the grid cutting and the measurement of the discrete fringe patterns are time consuming processes. The cost of the labor and machine is very high. A proposed study is the application of the heat treatment to the rails to release the residual stresses. A new technique of making gratings which can sustain high temperature is in progress. If the residual stress can be released by the annealing process, one can produce moire fringes throughout the specimen surface without breakage. As a result a much more detailed and accurate analysis can be made. Errors due to machining process will be completely circumvented. A continuous fringe pattern can be digitized and easily analyzed.

If the residual stresses are released by the heat treatment, laser speckle may also be used to investigate the released deformation. The surface of the slice of the rail can be treated by acid etching to generate suitable roughness so that a uniform speckle field can be attained under the illumination of a laser. Specklegrams are then to be taken before and after the annealing process. It is possible to obtain the displacement field by the whole field analysis of the sandwiched specklegrams. The advantage of laser speckle method is that the surface treatment of the specimen is simple and easy. However, the sensitivity and the accuracy of the measurement are lower than moire interferometry, and it needs post optical processing to extract the displacement contour maps.

6. ACKNOWLEDGEMENTS

This work was supported by DOT/RSPA Volpe National Transportation Systems Center. The authors which to thank Dr. Oscar Orringer of the Volpe Center and Dr. Roger K. Steele of the Association of American Railroads for their encouragement throughout the investigation and for correcting the manuscript and making valuable suggestions which were incorporated into the final report. The authors also wish to express their thanks to Mr. Biing-Ren Bih and Mr. Adam Trojanowski for their help in carrying out the specimen cutting process.

7. REFERENCES

1. Post D., "Moire interferometry," Chap. 7, *Handbook of Experimental Mechanics*, A.S. Kobayashi, Ed., Prentice Hall, Englewood Cliffs, NJ, 1987.

2. Czarnek, R., J. Lee and S.Y. Lin, "Moire interferometry and its potential for application to residual stress measurements in rails." *Residual Stress in Rails: Effects on Rail Integrity and Railroad Economics, Volume I - Field Experience and Test Results*, O. Orringer, J. Orkisz, and Z. Swiderski, Eds., Kluwer Academic Publishers, Norwell, MA, 1992, pp. 153-167.

3. Chiang F.P., "Moire methods of strain analysis," Chap. 6, *Manual of Experimental Stress Analysis*, 3rd ed. A.S. Kobayashi, Ed., Society for Experimental Stress Analysis, Bookfield Center, CT, 1978.

4. Malvern L.E., *Introduction to the Mechanics of a Continuous Medium*, Prentice-Hall, Englewood Cliffs, NJ, 1969.